

Stochastic Resonance Spectroscopy: Characterizing Fast Dynamics with Slow Measurements

Nicolaj Betz^{1,2}, Gregory McMurtrie¹, Max Hänze^{1,3}, Vivek Krishnakumar Rajathilakam¹, Laëtitia Farinacci^{1,4}, Susan N. Coppersmith⁵, Susanne Baumann¹ and Sebastian Loth^{1,2,3}

¹University of Stuttgart, Institute for Functional Matter and Quantum Technologies, 70569 Stuttgart, Germany.

²Center for Integrated Quantum Science and Technology (IQST), University of Stuttgart, 70569 Stuttgart, Germany.

³Max Planck Institute for Solid State Research, 70569 Stuttgart, Germany.

⁴Carl-Zeiss-Stiftung Center for Quantum Photonics Jena – Stuttgart – Ulm, Germany.

⁵School of Physics, University of New South Wales, Sydney, Australia.

ABSTRACT: A system's internal dynamics and its interaction with the environment can be determined by tracking how external perturbations affect its transition rates between states. However, accurately measuring these rates poses a significant challenge, especially when they span a wide range of time scales. Here we introduce a broadband measurement method, called stochastic resonance spectroscopy (SRS), that operates in the frequency domain and quantifies the stochastic dynamics of atomic-scale quantum systems. We apply this method to determine spin switching rates in a scanning tunneling microscope over an extremely wide frequency range, from 199 ms^{-1} for few-atom structures to 1.73 ns^{-1} for individual atoms. SRS relies on the universal phenomenon of stochastic resonance which synchronizes stochastic dynamics to an oscillating perturbation. We develop an analytical theory that extracts quantitative transition rates from scanning tunneling microscopy measurements of the frequency-dependent tunnel current and show that the signal is dominated by homodyne detection. Our theory indicates that SRS is not limited to spin dynamics and we corroborate this by measuring transport dynamics through a bound state in a superconductor. We anticipate that the ability to characterize broadband stochastic dynamics at the atomic scale will enable insights into excited-state dynamics of quantum systems and even non-Markovian processes emerging from correlations with the environment.

I. INTRODUCTION

Stochastic dynamics are ubiquitous in nature and crucial for understanding quantum systems at the atomic scale. A system's stochastic dynamics reflects the energy landscape of its states, the transition probabilities between them, and the system's interaction with the environment. Full characterization of these properties is typically accomplished through recording state trajectories that show the stochastic switching in real time [1, 2], which requires experimentally accessible observables to be recorded faster than the fastest rate of the system under investigation. Yet, detecting fast transition rates in nanoscale systems presents significant challenges arising from both instrumental and fundamental limitations. Measurable signals are often very small and require sensitive detection methods that are severely limited in temporal resolution [3]. In addition, intrinsic shot noise limits may make the measured quantity fundamentally inaccessible at sufficient signal-to-noise ratios [4, 5]. Despite these challenges, understanding and controlling such fast dynamics is crucial for many technological advancements, for example in spintronics, where magnetic switching occurs within picoseconds [6], or quantum computing, where qubit manipulation requires precise control at nanosecond speeds [7]. The continued shrinking of such technological devices to ever smaller length scales, and concomitant faster speeds requires experimental tools that overcome traditional detection limitations, and resolve fast dynamics of individual quantum systems at the atomic scale.

The scanning tunneling microscope (STM) is a prime tool to measure atomic-scale devices. To date, real-time measurements in STMs have directly resolved dynamics in larger nanostructures in the second to millisecond range. Examples are magnetization switching in nanometer-sized ferromagnetic islands [8, 9] and artificially assembled nanomagnets [10, 11, 12], as well as conformation switching of single-molecule devices [13, 14, 15] or charge switching of dopants in semiconductors [16]. In rare cases, specially designed environments enable millisecond-range transition rates of their spin or charge states even in single atoms [17, 18, 19, 20]. However, in most cases, the transition rates of individual quantum systems on surfaces are too fast to be tracked in real time [21, 22, 23]. Relaxometry methods such as pump-probe spectroscopy [24, 25, 26, 27], spin-echo measurements in electron paramagnetic resonance [28], or time-resolved luminescence [29, 30] typically resolve relaxation dynamics of the undriven systems, but characterizing fast driven dynamics of atomic-scale systems, i.e. systems that are excited by external drive signals, is technologically relevant, has yet to be explored.

Here, we show that quantitative information about the driven dynamics of an atomic-scale quantum system can be obtained from frequency-domain measurements with high fidelity and over a large range of timescales.

We exploit the phenomenon of stochastic resonance that appears in stochastically switching systems when a periodic perturbation of an external control parameter modulates the system's transition rates. [31, 32]. Stochastic resonance creates a characteristic frequency-dependent modification of the system's state evolution by synchronizing the switching events to the external perturbation. Stochastic resonance is typically observed by real-time measurements that detect the switching events directly. It has been found in a wide variety of driven classical systems from the earth's ice ages to the dynamics of neurons and electronic devices [33]. Recent experiments have verified the presence of stochastic resonance in time traces of slow spin switching of magnetic atoms [17], structural switching of atoms on 2D materials [34], and for single-electron levels of a quantum dot [35]. However, most atomic-scale objects have transition rates that are too fast for real-time observation because their transition rates are too fast.

Here, we exploit stochastic resonance’s synchronization between switching events and periodic perturbation to measure transition rates that are far faster than measurement acquisition times. This is possible because stochastic resonance affects time-averaged observables with a characteristic frequency dependence. When the external modulation is at a frequency that is much lower than the system’s intrinsic transition rates, the dynamics vary smoothly with the drive. In this slow modulation limit, the system’s response can be described by a slow oscillation of the steady-state occupation at the driving frequency. Conversely, when the driving frequency is much faster than the transition rates, multiple periods of the external modulation occur between each transition. In this fast-modulation limit, the system’s response is well-described by random switching according to modified non-oscillatory transition rates and the oscillation of the state occupation at the driving frequency vanishes. This cross-over from oscillatory to non-oscillatory state occupation can be detected in any observable that depends on the state occupation. As a consequence, slowly sweeping the frequency of the periodic perturbation and recording the resulting change in the time-averaged state-dependent observable enables spectroscopic measurement of the system’s transition rates. We term this method *stochastic resonance spectroscopy (SRS)*.

We develop an analytical theory for SRS that fits measured spectra quantitatively and extracts switching rates from the driven stochastic dynamics of atomic-scale objects with high accuracy. We implement SRS in a scanning tunneling microscope where an oscillating bias voltage serves as periodic drive and the tunnel current is the state-dependent observable. A single SRS measurement can characterize stochastic dynamics with time constants ranging from milliseconds to picoseconds. Specifically, we apply SRS to measure magnetic transitions of single atoms on a surface and resolve stochastic switching between individual spin states on time scales as short as 580 ps. We find that the analytical model holds over a large range of modulation amplitudes and for a variety of rate configurations of the spin system under investigation and that SRS can even resolve which spin states participate in the dynamics. Comparison to a numerical simulation using master rate equations confirms that SRS characterizes these spin systems quantitatively. Finally, we measure the quasiparticle dynamics of a bound state on a superconducting substrate by SRS and thus demonstrate that the SRS method and corresponding theory is applicable far beyond spin systems on surfaces.

II. STOCHASTIC RESONANCE SPECTROSCOPY IN SPIN SYSTEMS

In stochastic resonance spectroscopy (SRS) of spin systems, measured using spin-dependent scanning tunneling microscopy (STM), we apply an AC driving voltage, V_{ac} , at frequency f and record the impact of varying the frequency of this electrical drive on the time-averaged tunnel current. To separate the stochastic resonance signal (SRS signal) produced by the microwave modulation from other components of the tunnel current, we chop the microwave modulation on and off at 691 Hz and detect the resulting variation in the tunnel current using a lock-in amplifier. We use a spin-polarized tip to become sensitive to the spin system’s states by tunnel magnetoresistance [36]. The resulting SRS signal as a function of drive frequency is shown in Fig.1 for two different spin systems: an individual Fe atom on a Cu binding site on $\text{Cu}_2\text{N}/\text{Cu}(100)$ (light blue) and a chain of 4 such atoms on the same substrate (dark blue). For logarithmically spaced frequency steps, the SRS signal appears as a single step that smoothly transitions between two levels over approximately one order of magnitude in frequency. We

find that the step has the same shape and width for both systems but is centered at 31.7 kHz for the linear chain of four Fe atoms and at 0.27 GHz for the individual Fe atom. The change in characteristic frequencies between the chain and atom matches the difference of transition rates estimated from spin state lifetimes of similar structures reported in literature [37, 10].

The universal signal shape of SRS is a consequence of stochastic resonance behavior and features a quantitative relation between the characteristic frequency of the signal step in SRS and the transition rates of the driven system. This relation is not limited to spin systems as will be shown below (Section V).

An analytic expression for the SRS signal shape in Fig. 1 can be obtained with minimal assumptions by considering the behavior of a general two-level system with Markovian transition rates. The harmonic drive voltage modulates the excitation Γ_+ and relaxation Γ_- rates of the spin system, and they become time- and frequency-dependent: $\Gamma_{\pm}(V) = \Gamma_{\pm}(V_{dc} + V_{ac} \cdot \cos(2\pi ft))$. This provides periodic intervals in time when the switching between spin states is enhanced (Fig. 2a). As a result, the occupation probabilities of the spin states oscillate in time with oscillation amplitude and phase that depend on f (Fig. 2b). Due to the tunnel magnetoresistance effect, the tunnel junction conductance depends on the spin orientation of the atom below the tip, i.e. the state occupation. The tunnel current contains a product of both the bias voltage (yellow) and occupation probabilities (blue): $I = (V_{dc} + V_{ac} \cdot \cos(2\pi ft))(\sigma_g + \Delta\sigma \sum n_q(f)e^{2\pi i q f t})$, where σ_g is the conductance of the ground state, $\Delta\sigma$ is the conductivity difference between excited and ground state and $\sum n_q(f)e^{2\pi i q f t}$ is the occupation probability of the excited state expanded in its Fourier series (see Supplemental Material for details [38]).

Herein lies the strength of SRS: the fast stochastic dynamics of the system contribute to the tunnel current in two ways, via the average occupation ($q = 0$ term) weighted by V_{dc} , and the first harmonic ($q = \pm 1$ terms), which down-mixes with V_{ac} . Both produce a tunnel current component that is detectable in slow measurements at d.c. with a conventional current amplifier, even if the state occupation itself oscillates at very high frequency.

For the general case of a two-state system with Markovian transition rates, we derive in Supplemental Material section 1 [38], that up to 2nd order all three terms combined ($q = 0, -1, +1$) lead to the frequency-dependent SRS signal (Fig. 2c)

$$I(f) = I_{SR} \frac{1}{\Omega^2 + 1} + I_{rec} = I_{SR} \frac{\Gamma^2}{\Gamma^2 + (2\pi f)^2} + I_{rec},$$

[1]

where the I_{SR} represents the height of the observed step, I_{rec} is the offset current and $\Omega = 2\pi f/\Gamma$. Importantly, Γ is the sum of the time-averaged transition rates of the two-level system $\Gamma = \langle \Gamma_+(t) + \Gamma_-(t) \rangle$. On a logarithmic frequency scale, the Lorentzian function of eq. 1 appears as a step with fixed width that has its inflection point at $\Omega = 1$, where the external drive frequency matches exactly to the characteristic transition rate of the system. Hence, determining the inflection point's frequency, f_{Γ} , in a SRS measurement quantitatively measures the transition rates of the system of interest as $\Gamma = 2\pi f_{\Gamma}$.

Fitting the experimental data in Fig. 1d with eq. 1 (solid lines) yields a switching rate of $\Gamma_{Fe} = (1.73 \pm 0.04) \cdot 10^9/s$ for the single Fe atom and $\Gamma_{4Fe} = (199 \pm 5) \cdot 10^3/s$ for the Fe chain. The switching rate for the single Fe atom determined in this manner is consistent with switching rate that we obtained by performing all-electronic pump probe measurements on an Fe atom, which yielded a spin relaxation time of 0.6 ± 0.1 ns corresponding to a relaxation rate of $\Gamma_{-,Fe} = (1.7 \pm 0.4) \cdot 10^9/s$ (Supplementary Fig. S1 [38]). The results agree within their error bars, but the SRS measurement provides significantly tighter confidence intervals because signal quality is improved when performing frequency-domain measurements compared to pulsed experiments with nanosecond pulses.

It is worth noting that the SRS signal is often dominated by the down-mixed component ($q = \pm 1$, see section III). This component comprises the occupation probability that oscillates in phase with the drive (the real part of $n_{\pm 1}$). It can be understood as homodyne detection of the occupation [39]. Higher harmonic terms with $|q| > 1$ oscillate at multiples of the drive frequency and usually do not mix to a detectable tunnel current.

The offset current, I_{rec} , contains all frequency-independent contributions to the occupation, and also the rectification of the microwave modulation due to a non-linear IV characteristic. But these terms only add a constant offset to the SRS signal, provided that the transfer function of the bias voltage has been flattened [40, 37, 41] to ensure constant-amplitude driving at all frequencies prior to the SRS measurements.

The SRS signal amplitude, I_{SR} , can have either sign, depending on the bias polarity and the sign of $\Delta\sigma$, and additional information about the spin system can be extracted from this change of polarity (see section IV.A).

The measurements in Fig. 1 demonstrate the large dynamic range of SRS and highlight that its universal lineshape enables quantitative measurements of transition rates with high accuracy: the switching rates of the individual Fe atom and the Fe chain differ by four orders of magnitude, yet both rates are measured with an uncertainty of only 2% of the fitted rate.

III. STOCHASTIC RESONANCE SPECTROSCOPY OF TWO-STATE SYSTEMS

In our analytical model of SRS, we consider the frequency dependence of the occupation probabilities of the spin states. We now delve deeper into the analytical model introduced with eq.1 and characterize the range of its applicability beyond spin systems.

Using the two-state Markov chain model, the occupation probability of both states can be obtained by solving two integrals that depend on the excitation rate $\Gamma_+(t)$ and the sum of the excitation and relaxation rates $\Gamma(t) = \Gamma_+(t) + \Gamma_-(t)$ [32]. Using the Fourier series of $\Gamma(t)$ and $\Gamma_+(t)$ it is possible to solve these integrals analytically and obtain the exact time-dependent occupation probability for arbitrary transition rates (see Supplemental Material [38]). Considering the lowest order contribution to this general solution, i.e. when $\Gamma(t) = \Gamma$ is constant in time, the occupation probability is

$$n(t) = \sum_q \frac{a_q}{\Gamma} \frac{1 - iq\Omega}{q^2\Omega^2 + 1} e^{iq\Omega t},$$

[2]

where a_q are the Fourier coefficients of the excitation rate and $q = 0, \pm 1, \pm 2, \dots$. Eq. 2 directly quantifies the qualitative description discussed above (Fig. 2): at low frequencies, $\Omega \ll 1$, the solution reduces to the adiabatic steady-state solution $n(t) = \Gamma_+(t)/\Gamma$ in which the switching follows the drive oscillation; and at high frequencies, $\Omega \gg 1$, eq. 2 approaches $n(t) = a_0/\Gamma = \langle \Gamma_+(t) \rangle / \Gamma$, which is not time-dependent and describes the loss of synchronization with the drive oscillation¹. The transition between these low and high frequency limits follows a Fourier series in which the q^{th} harmonic of the drive frequency has an amplitude a_q/Γ that decays as $1/\sqrt{q^2\Omega^2 + 1}$ and has a frequency-dependent phase shift $\arctan(q\Omega)$, yielding an in-phase component of the occupation probability with a Lorentzian decay $\propto 1/(q^2\Omega^2 + 1)$.

Eq. 2 also specifies why the homodyne component is typically the dominant contribution to the SRS signal. The time-average occupation probability ($q = 0$) is given by $n_0 = a_0/\Gamma$ and does not depend on frequency. It creates a constant offset that enters I_{rec} . By contrast, the homodyne signal ($q = \pm 1$) is given by the in-phase part of the first harmonic $n_{\pm 1} = a_{\pm 1}/\Gamma \cdot 1/(\Omega^2 + 1)$ and produces the characteristic lineshape of SRS

$$I^{\Gamma=const.} = \Delta\sigma V_{ac} \frac{a_{\pm 1}}{\Gamma} \frac{1}{\Omega^2 + 1} + I_{rec}.$$

[3]

We find that eq. 3 gives the same lineshape as eq. 1 and quantifies the SRS magnitude in terms of the Fourier components of the transition rates. The case considered so far, where $\Gamma(t) = \Gamma$, is a good approximation as long as the modulation of the rates remains small compared to the intrinsic rates, this is encountered in a large range of physical systems such as the one shown in Fig. 5 below.

Nevertheless, in other systems or under specific drive conditions, the excitation and relaxation rates may modulate such that $\Gamma(t)$ is far from constant. This occurs, for example, when the oscillatory drive is crossing an energy threshold of a system with more than two states or when the drive amplitude is very large. Yet, as we show next, even with sizeable modulations, e.g. in the measurement shown in Fig. 1, the SRS lineshape is still well-described by eq.1.

In general, a time dependent $\Gamma(t)$ causes higher order terms that may distort the Lorentzian lineshape of the SRS signal, as displayed in Supplementary Fig. S4c-f [38]. These distortions are caused by a mixing of different harmonics which give rise to a series of terms where the j^{th} term scales with $O\left(\frac{a_k}{\Gamma} \prod_{i=1}^{j-1} \frac{b_{m_i}}{\Gamma}\right)$, where $k = q - \sum_{i=1}^{j-1} m_i$, and $\{m_i\}$ is a set of $j - 1$ integers (see Supplemental Material [38] for details). These terms have the same Lorentzian shape as the terms in eq. 2. but may be shifted towards lower frequencies.

¹ Both limits can also be obtained for time-dependent $\Gamma(t)$ (see Supplemental Material, section 2 [38]).

Interestingly, the first Fourier components ($|k| \leq 1$) of the 2nd order terms do not distort the SRS lineshape. As a result, we find that in the simplest case of linear dependence of the rate with drive amplitude, such distortions remain negligible up to moderately large modulations, relative to the time-average transition rate $\Gamma = \langle \Gamma(t) \rangle$. Linear modulations of $\Gamma(t)$ up to 60% lead to an underestimation of Γ of only 5% (See Supplementary Fig. S5 [38]). This is comparable to the experimental noise of a typical SRS measurement and therefore an acceptable deviation. More stringent limitations apply to systems with a highly non-linear drive dependence, e.g. when the modulation crosses an energy threshold, as set by inelastic excitations in spin systems (see Section IV below). This non-linearity enhances the contribution of higher order terms and thus requires smaller drive amplitude to avoid distortions. Measurements in the higher order regime are identifiable by visible deviations from the normal SRS lineshape defined in eq.1 (see Supplementary Fig. S4a,b [38] for examples).

IV. STOCHASTIC RESONANCE SPECTROSCOPY OF MULTI-STATE SPIN SYSTEMS

In Sec. III above, we examined the SRS signal based on a general two-level system and discussed the regime in which the modulation of the rates is purely linear with drive amplitude. However, real spin systems often exhibit multiple energy levels, and modulating across them leads, in general, to a nonlinear time-dependence of the rates. Here, we illustrate how SRS can be used to explore these thresholds for the example case of the single Fe atom on Cu₂N/Cu(100) that features five spin states which are all connected by different transition rates. To that end, we compare offset voltage and modulation amplitude dependent measurements with a numerical model of the Fe atom's spin dynamics (see Supplemental Material, section S3 [38]). Despite the complexity of the five-state spin system, we find that the Fe atom's driven dynamics, and corresponding SRS signal, can be mapped back onto those of a two-level system with adjusted transition rates (solid lines in Fig. 3b,d-f).

The mapping of the Fe atom's properties to a two-level system makes it possible to use the analytical model introduced in section III. The resulting SRS signal varies with offset bias and modulation amplitude (solid lines in Fig. 3b,d-f) and closely matches to the signal obtained from the numerical simulation of the full five-state system (dashed lines in Fig. 3b,d-f), highlighting the general applicability of the SRS lineshape (eq. 1).

A. Amplitude-dependence of the SRS signal

We treat the Fe atom as a spin of magnitude 2 with easy-axis and transverse magneto-crystalline anisotropy, weakly coupled to a metallic surface through a thin insulating [42]. A magnetic field is applied parallel to the easy magnetic axis² and leads to the spin state energies depicted in Fig. 3c. Two states with $\langle S_z \rangle \approx \pm 2$ are at low energy and separated by three higher excited states with $\langle S_z \rangle < 1$. Finite transverse magnetic anisotropy enables inelastic electron scattering between all spin states with drastically varying transition rates [43]. Up to a voltage threshold, V_{th} , transitions occur directly between the two low-energy spin states and mapping to a two-level system is straightforward. The

² The tip's spin polarization is assumed to be parallel to the magnetic field for simplicity.

transition rates are essentially independent of the bias voltage and determined only by environmental influences such as thermal noise [10]. Above the threshold, inelastic excitations to the higher excited states become available and drastically increase the effective transition rates between the two low-energy states. The increase with bias voltage is mostly linear because spin transitions due to inelastic electron tunneling between tip and sample increase linearly with excess voltage. The imbalance between excitation (blue) and relaxation (red) rates above the threshold is a direct consequence of the tip spin polarization [44]. Spin polarized tunneling depends on the alignment between tip and surface spin and the direction of tunneling respectively, and makes certain transitions more likely than others.

For the mapping onto an effective two-level system treatment of the Fe atom, we keep the two low-energy states, $\langle S_Z \rangle = \pm 2$, that correspond to opposite magnetizations of the Fe atom. The higher excited states are treated as transient states that modify the voltage-dependence of the rates between the $\langle S_Z \rangle = \pm 2$ states. Specifically, we calculate the rates of transitions from the ground into the higher excited states and weight them with the probability of reaching the first excited state (and vice versa). Then, the microwave drive, consisting of the offset voltage, V_{dc} , and drive amplitude, V_{ac} , modulates the transition rates between the two low-energy states according to this voltage dependence, Fig. 3a.

We find that varying the drive amplitude V_{ac} while keeping the offset V_{dc} constant yields information on the rate modulation and the modulation regime of SRS (Fig. 3b, solid line). As long as the drive amplitude is small and the peak applied voltage does not overcome the excitation threshold $V_{dc} + V_{ac} < V_{th}$ (marked by a grey line), the system does not react to the driving and the SRS measurement will show no step, i.e. the signal amplitude I_{SR} vanishes. For larger drive amplitudes, the SRS signal increases almost quadratically with modulation amplitude (see black fitted line). The measurable signal consists of the homodyne signal in lowest order $\Delta\sigma V_{ac} \cdot a_{\pm 1}/\Gamma$ and depends on the Fourier component of the rate that oscillates with the drive frequency. This Fourier component increases linearly with drive amplitude ($a_{\pm 1} \sim V_{dc} + V_{ac} - V_{th}$) while the average rate Γ stays constant. Thus, the initially quadratic behavior indicates that the spin system is driven in the weak modulation regime where the lowest order approximation of the SRS signal holds. Deviations from the quadratic trend appear toward higher modulation amplitudes and indicate the transition to the regime of strong modulation where higher order effects become relevant. However, as shown in Supplementary Fig. S6c,d [38], the main contribution to these deviations are the terms with $j = 2$ and $|k| < 2$ which do not distort the SRS signal, i.e. the transition rate in this regime is still measured accurately.

Varying the drive offset, V_{dc} , while keeping the drive amplitude constant (Fig. 3d) shows a positive peak in the signal amplitude I_{SR} for negative drive offset and a negative peak for positive offset. The reversed sign and reduced magnitude of the peak at positive bias compared to that at negative bias is a consequence of the asymmetry in the excitation rate and thus carries information about the spin polarization of the excitation. The signal amplitude rises sharply when the bias voltage $V_{dc} \pm V_{ac}$ modulates around the excitation threshold and decays towards higher drive offsets. During this decay, the modulation of the rate $a_{\pm 1}$ in our analytical model is constant while the average rate Γ increases linearly. In lowest order, this leads to a decay of the form $\sim 1/(V_{dc} - \beta)$ (where β is a fitting parameter) which qualitatively fits the observed behavior. Deviations are, again, caused by higher order contributions to the SRS signal (Supplementary Fig. S6a,b [38]). We find that the offset voltage at which the signal peaks depends on the modulation regime, but the position of the signal onsets appears at $|V_{dc}| = V_{th} - V_{ac}$ for both bias polarities and is fixed to the excitation threshold. Hence, in general,

observing an increase in signal amplitude as a function of drive offset indicates an excitation threshold of the spin system at that voltage.

Experimentally, we find that sweeps of the offset voltage often show more than one threshold in spin systems. For example, Fig. 3f shows a drive offset sweep for the Fe atom on Cu₂N in which two excitation thresholds appear (light blue dots). One highly asymmetric threshold leads to a peak at approximately $V_{dc} \approx -5 \text{ mV}$. The corresponding dip at positive offset vanishes in the peak-dip structure at $V_{dc} \approx \pm 2 \text{ mV}$ of the second lower energy threshold. Since the threshold of this second spin transition is smaller than V_{ac} , the signal onsets at positive and negative bias merge, leading to a smooth change in signal across zero bias. This double-threshold behavior fits well to the step-like changes in the differential conductance observed at the same voltages with inelastic electron tunneling spectroscopy (Supplementary Fig. S2 [38]) and is thus an alternative way to gain information on the energies of the spin transitions in such atoms, which is especially interesting because not all atoms or spin transitions show inelastic electron tunneling excitations [45].

B. Threshold behavior

To understand the double-threshold behavior shown in Fig. 3f, we expand the description of the Fe atom to a master rate equation that includes all five spin states and treats the voltage-dependent modulation of their transition rates according to established first order scattering theory [43], Fig. 3c. Time-evolving the rate equation directly yields the time-dependent occupation probability for all five states and the state-dependent tunneling rates that convert the oscillating occupation to a time-dependent tunnel current (see Supplemental Material, section S3 for details [38]). Within the rate equation model, the SRS signal is the difference between the time-average of this oscillating tunnel current and the tunnel current of the system with a time-independent voltage V_{dc} . The numerically calculated SRS signal quantitatively reproduces the measured SRS lineshape on the Fe atom of Fig. 1d, shown in Fig. 3e for $V_{dc} = -5.5 \text{ mV}$. This indicates that the frequency-dependent SRS signal closely follows the Lorentzian-like shape of eq. 1, even though five rather than two states are participating in the dynamics.

The five-state simulation also fits the measured variation of the SRS signal with drive offset voltage and reproduces the peak-dip structures of both thresholds quantitatively (Fig. 3f, green dashed curve). This enables the identification of the spin states that participate in the magnetization reversal of the Fe atom. Simulating only the ground and first excited state creates a weak SRS signal (Fig. 3e, yellow dashed curve) and reproduces the peak-dip feature at $\pm 2 \text{ mV}$ (Fig. 3f, yellow dashed curve) indicating that it results from direct transitions between the two low-energy spin states of the easy-axis spin system. Including the second excited state, which lies 4 mV above the ground state, increases the SRS amplitude making it comparable to the measured one (Fig. 3e, red dashed curve). It also creates the peak in SRS signal at -5 mV (Fig. 3f, red dashed curve), and corresponds to excitations over the anisotropy barrier via higher excited spin states. The third excited state at 6 mV above the ground state is then required to correctly reproduce the signal decay to higher offset voltages (Fig. 3f, blue curve).

Comparing the full five-state model to the reduced two-level description shows that signal amplitudes of the two-level model are up to 10% larger than those of the full simulation, but the characteristic frequency of the resulting SRS steps, i.e. the Fe atom's average transition rates, agree within <2% with the full five-state calculation. The rate obtained by fitting the full simulation with eq. 1 is $1.77 \cdot 10^9/\text{s}$, and the rate of the effective two state system is $1.74 \cdot 10^9/\text{s}$. This highlights that straightforward fitting

of SRS signals with eq. 1 yields accurate rates even in multi-state spin systems. It further shows that no prior knowledge about the energy landscape of a system is required in order to measure its dynamics with SRS.

C. Transition rates

An important consequence of the threshold behavior of the SRS response at the Fe atom's transition rates is that different regimes of the stochastic dynamics may be studied in different intervals of the drive offset voltage. This becomes apparent when analyzing the transition rates as a function of offset voltage for small drive amplitudes (Fig. 4).

For low offset voltages ($V_{dc} < \pm 4$ mV), the measured transition rates are approximately constant at $\Gamma = (1.4 \pm 0.1) \cdot 10^9/s$ (Fig. 4 blue dots). This indicates that the rate is dominated by transitions that do not depend on the applied bias. The full five-state calculation as well as the effective two-state model match this behavior well apart (Fig. 4 dashed and solid lines). The spin transitions in this range of offset voltages are the direct tunneling of magnetization transitions between the ground and the first excited state, $\langle S_Z \rangle = \pm 2$, for which the rate-determining process is inelastic scattering of electrons from the substrate rather than tunneling between tip and sample. The measured rate at low offset voltage is therefore a good approximation to the intrinsic switching rate of the Fe atom when it is not driven by external perturbation.

When the offset voltage exceeds the excitation threshold at $V_{dc} > \pm 4$ mV, the measured transition rate increases substantially with offset voltage magnitude. This indicates that a new transition pathway becomes available that involves spin transitions driven by tunneling electrons, because the rate of electron tunneling increases with increasing offset voltage. The numerical model reproduces the increasing transition rate only when the second excited state at 4 meV above the ground state is included in the rate calculation (Fig. 4 red curve). The rate of increase changes at ± 5.5 mV. The numerical simulations show that transitions via the 3rd excited state must be included to reproduce this change in rates (Fig. 4 blue curve). Towards even higher offset voltage the transition rate of the Fe atom increases linearly by $0.36 \cdot 10^9 s^{-1} mV^{-1}$ for positive offset voltage and by $0.29 \cdot 10^9 s^{-1} mV^{-1}$ for negative offset voltage. Relative to the tunnel junction setpoint of 1 nA at 10 mV, the electron tunneling rate increases approximately by $0.6 \cdot 10^9 s^{-1} mV^{-1}$, which indicates that the transition pathways through the higher excited state flip the Fe atom's magnetization very efficiently.

The measurements shown in Fig. 4 demonstrate that SRS is capable of accurately tracking the driven dynamics of a quantum system. The Fe atom on Cu₂N/Cu(100), that was measured here, is a well-studied model system. The comparison between measured and calculated bias dependence of the transition rates highlights how tracking variations of the transition rates and signal amplitudes resolves changes in the relevant transition pathways between the system's states. SRS thus provides spectroscopic insights into the underlying switching processes between all relevant states of a quantum system.

We note that the simulation shown in Fig. 3 displays a sharp feature at +5.0 mV, which we suspect occurs when two transition pathways have the same rate and block each other. While the small SRS signal amplitudes in that bias region do not allow us to definitively resolve this feature, it opens up an interesting pathway for future SRS investigations of potential destructive interferences between transport channels.

V. GENERALITY OF THE STOCHASTIC RESONANCE SPECTROSCOPY METHOD

SRS is a powerful technique for measuring a system's dynamics over a wide frequency range. Importantly, SRS has only two requirements: (i) the transition probabilities between the investigated states of the system must depend on an external control parameter that can be modulated at different frequencies and (ii) it must be possible to record the time average of an observable that depends on the state of the investigated system. For spin systems studied by inelastic electron tunneling, we have shown above that the transition probabilities can be modulated by the bias voltage, and that, by using a spin-polarized tip, one can measure the spin-polarized tunnel current, which depends on the spin state of the system.

The requirements for SRS can be met in a much larger range of systems with stochastic dynamics. We demonstrate this by applying the SRS measurement scheme to Yu-Shiba-Rusinov (YSR) states [46, 47, 48]. The tunneling dynamics through YSR states are an example of transport dynamics through discrete states. YSR states are bound states inside a superconductor created by exchange scattering at magnetic impurities. Evaporating Fe atoms onto V(100) leads to the presence of YSR states that appear as peak-dip features in differential conductivity spectra, dI/dV , inside the superconducting gap when measured with a superconducting tip (Fig. 5, inset).

Occupying a YSR state requires a minimal excitation energy that can be supplied by an external voltage. Modulating this voltage thus modulates the probability of occupying the state, satisfying requirement (i). Additionally, previous studies have shown that the tunnel current is directly sensitive to the occupation of the state [49], which satisfies requirement (ii).

SRS measurements with offset voltage adjusted to the low-voltage edge of the YSR state and a drive amplitude comparable to the state's width (sketched by yellow oscillation in the inset of Fig. 5) results in a clear SRS signal (Fig. 5, blue dots). The measured lineshape is well described by eq. 1, which allows a precise fit of the YSR state's transition rate $\Gamma_{\text{YSR}} = 4.91 \pm 0.06 \cdot 10^9/\text{s}$. This rate agrees with estimates obtained by tuning the tunnel junction conductance as in [49] (see Supplementary Fig. S7 [38]). It corresponds to a YSR state lifetime of 204 ± 4 ps which is much shorter than that expected from Fermi-Dirac statistics at our measurement temperature (50 mK). A similar discrepancy was also found in previous studies of YSR lifetimes that used junction conductance estimates or shot noise measurements [49, 50, 51].

The origin of such low lifetimes remain elusive, and additional data will be needed to gain insights into the physics at play. SRS offers the advantage that the dynamics of the YSR states can be measured for fixed tip height and bias voltage. This enables future experiments in which the influence of the tip on the YSR state may be resolved or even leveraged to tune other key parameters such as the YSR state energy.

This example demonstrates the broad application range of SRS beyond spin dynamics and we expect that SRS can be used in STM to investigate the dynamics of a wide variety of other discrete systems such as the dynamics of orbitals, charge states, quasi-particle lifetimes in atoms, molecules or other 0D defects, and ultrafast dynamics emerging from strong correlations with a bath [52]. Shifting away from observing dynamics via the tunneling current, SRS may also be implemented using luminescence as the

observable, enabling the measurement of localized exciton dynamics in an STM. The universality of stochastic processes further makes SRS potentially applicable to other research fields that go beyond STM investigations, for example studies in quantum dots [35]. Additionally, SRS bears some similarity to AC susceptibility measurements that are frequently used in the characterization of ensembles of molecular magnets and molecular qubits [53, 54, 55]. We therefore anticipate that SRS will also allow for new types of single-molecule studies on surfaces and open up possibilities for the investigation of coupled spin or molecular systems.

VI. CONCLUSION

We introduce a new broadband microwave spectroscopy method, called stochastic resonance spectroscopy (SRS), that provides direct experimental access to the switching dynamics of atomic-scale structures in a scanning tunneling microscope. By adding a small oscillating voltage to the conventional bias we create a frequency-dependent variation in the time-averaged tunnel current that makes the characteristic transition rates of ultrafast stochastic switching detectable with the slow low-bandwidth electronics of an STM. We find that SRS features a unique combination of large dynamic range and high accuracy for measurements of the internal dynamics of nanoscale or quantum systems with discrete states. SRS is well-suited to study driven dynamics because it does not require unperturbed evolution of the system under investigation.

We develop an analytical description of the SRS lineshape that is based on the driven stochastic dynamics of a generic two-level system. This lineshape accurately fits measured SRS signals even for systems that have more than two states and it holds for a large range of experimental settings. It has a universal Lorentzian shape as long as the periodic perturbation by the external harmonic drive is small enough to remain in the linear response regime. Distorted lineshapes indicate deviations from this small-modulation regime.

The SRS lineshape is defined by three parameters: characteristic frequency, signal amplitude and measurement offset. The characteristic frequency is a direct measure of the sum of transition rates of the investigated system. The signal amplitude comprises homodyne detection of the oscillating occupation probability of the periodically driven system and its frequency-dependent variation of the time-averaged occupation probability. Variations in SRS signal amplitude with changing bias offset voltage indicate crossovers between different transition pathways and provide detailed spectroscopic information about the investigated atomic-scale system.

In conclusion, SRS resolves dynamics over a broad range of timescales, and we present measurements that range between several microseconds for the spin switching of a few-atom nanostructure to a few hundred picoseconds for the tunneling dynamics of a bound state in a superconductor. We expect that even faster timescales will be accessible with this technique because the method is, in principle, only limited by the bandwidth of the microwave generator used, and that the technique will be highly useful for other types of stochastically switching systems.

ACKNOWLEDGEMENTS

N.B. acknowledges support from the Carl-Zeiss-Stiftung, the Centre for Integrated Quantum Science and Technology (IQST). L.F. acknowledges support from the Carl-Zeiss-Stiftung, CZS Center QPhoton. S.N.C. acknowledges support from the US Army Research Office, Award #W911NF-23-1-0110 and from the Australian Research Council, Project No. DP210101608. S.B. and S.L. acknowledge support from the Baden Württemberg Foundation Program on Quantum Technologies (Project AModiQuS).

REFERENCES

- [1] M. B. Plenio and P. L. Knight, The quantum-jump approach to dissipative dynamics in quantum optics, *Rev. Mod. Phys.* **70**, 101 (1998).
- [2] U. Seifert, Stochastic thermodynamics, fluctuation theorems and molecular machines, *Rep. Prog. Phys.* **75**, 126001 (2012).
- [3] G. Giusi, G. Cannatà, G. Scandurra and C. Ciofi, Ultra-low-noise large-bandwidth transimpedance amplifier, *Int. J. Circ. Theor. Appl.* **43**, 1455 (2014).
- [4] R. Gao, M. A. Edwards, J. M. Harris and H. S. White, Shot noise sets the limit of quantification in electrochemical measurements, *Curr. Opin. Electrochem.* **22**, 170 (2020).
- [5] A. V. der Ziel, *Noise in solid state devices and circuits* (Wiley, New York, 1986).
- [6] K. Jhuria, J. Hohlfeld, A. Pattabi, E. Martin, A. Y. Arriola Córdova, X. Shi, R. Lo Conte, S. Petit-Watelot, J. C. Rojas-Sanchez, G. Malinowski, S. Mangin, A. Lemaître, M. Hehn, J. Bokor, R. B. Wilson and J. Gorchon, Spin-orbit torque switching of a ferromagnet with picosecond electrical pulses, *Nat. Electron.* **3**, 680 (2020).
- [7] Y. Chew, T. Tomita, T. P. Mahesh, S. Sugawa, S. de Léséleuc and K. Ohmori, Ultrafast energy exchange between two single Rydberg atoms on a nanosecond timescale, *Nat. Photonics* **16**, 724 (2022).
- [8] S. Krause, L. Berbil-Bautista, G. Herzog, M. Bode and R. Wiesendanger, Current-Induced Magnetization Switching with a Spin-Polarized Scanning Tunneling Microscope, *Science* **317**, 1537 (2007).
- [9] L. Gerhard, T. K. Yamada, T. Balashov, A. F. Takács, R. J. H. Wesselink, M. Däne, M. Fechner, S. Ostanin, A. Ernst, I. Mertig and W. Wulfhekel, Magnetoelectric coupling at metal surfaces, *Nat. Nanotechnol.* **5**, 792 (2010).
- [10] S. Loth, S. Baumann, C. P. Lutz, D. M. Eigler and A. J. Heinrich, Bistability in Atomic-Scale Antiferromagnets, *Science* **335**, 196 (2012).
- [11] A. Spinelli, B. Bryant, F. Delgado, J. Fernández-Rossier and A. F. Otte, Imaging of spin waves in atomically designed nanomagnets, *Nat. Mater.* **13**, 782 (2014).
- [12] A. A. Khajetoorians, B. Baxevanis, C. Hübner, T. Schlenk, S. Krause, T. O. Wehling, S. Lounis, A. Lichtenstein, D. Pfannkuche, J. Wiebe and R. Wiesendanger, Current-Driven Spin Dynamics of Artificially Constructed Quantum Magnets, *Science* **339**, 55 (2013).

- [13] L. Gao, Q. Liu, Y. Y. Zhang, N. Jiang, H. G. Zhang, Z. H. Cheng, W. F. Qiu, S. X. Du, Y. Q. Liu, W. A. Hofer and H.-J. Gao, Constructing an Array of Anchored Single-Molecule Rotors on Gold Surfaces, *Phys. Rev. Lett.* **101**, 197209 (2008).
- [14] P. Liljeroth, J. Repp and G. Meyer, Current-Induced Hydrogen Tautomerization and Conductance Switching of Naphthalocyanine Molecules, *Science* **317**, 1203 (2007).
- [15] J. L. Zhang, J. Q. Zhong, J. D. Lin, W. P. Hu, K. Wu, G. Q. Xu, A. T. S. Wee and W. Chen, Towards single molecule switches, *Chem. Soc. Rev.* **44**, 2998 (2015).
- [16] K. Teichmann, M. Wenderoth, S. Loth, J. K. Garleff, A. P. Wijnheijmer, P. M. Koenraad and R. G. Ulbrich, Bistable Charge Configuration of Donor Systems near the GaAs(110) Surfaces, *Nano Lett.* **11**, 3538 (2011).
- [17] M. Hänze, G. McMurtrie, S. Baumann, L. Malavolti, S. N. Coppersmith and S. Loth, Quantum stochastic resonance of individual Fe atoms, *Sci. Adv.* **7**, eabg2616 (2021).
- [18] I. G. Rau, S. Baumann, S. Rusponi, F. Donati, S. Stepanow, L. Gragnaniello, J. Dreiser, C. Piamonteze, F. Nolting, S. Gangopadhyay, O. R. Albertini, R. M. Macfarlane, C. P. Lutz, B. A. Jones, P. Gambardella, A. J. Heinrich and H. Brune, Reaching the magnetic anisotropy limit of a 3 d metal atom, *Science* **344**, 988 (2014).
- [19] B. Kiraly, A. N. Rudenko, W. M. J. van Weerdenburg, D. Wegner, M. I. Katsnelson and A. A. Khajetoorians, An orbitally derived single-atom magnetic memory, *Nat. Commun.* **9**, 3904 (2018).
- [20] S. Fatayer, F. Albrecht, I. Tavernelli, M. Persson, N. Moll and L. Gross, Probing Molecular Excited States by Atomic Force Microscopy, *Phys. Rev. Lett.* **126**, 176801 (2021).
- [21] S. Loth, K. von Bergmann, M. Ternes, A. F. Otte, C. P. Lutz and A. J. Heinrich, Controlling the state of quantum spins with electric currents, *Nat. Phys.* **6**, 340 (2010).
- [22] J. Hermenau, M. Ternes, M. Steinbrecher, R. Wiesendanger and J. Wiebe, Long Spin-Relaxation Times in a Transition-Metal Atom in Direct Contact to a Metal Substrate, *Nano Lett.* **18**, 1978 (2018).
- [23] C. Lotze, M. Corso, K. J. Franke, F. von Oppen and J. I. Pascual, Driving a Macroscopic Oscillator with the Stochastic Motion of a Hydrogen Molecule, *Science* **338**, 779 (2012).
- [24] S. Loth, M. Etzkorn, C. P. Lutz, D. M. Eigler and A. J. Heinrich, Measurement of Fast Electron Spin Relaxation Times with Atomic Resolution, *Science* **329**, 1628 (2010).
- [25] C. Saunus, J. Raphael Bindel, M. Pratzer and M. Morgenstern, Versatile scanning tunneling microscopy with 120 ps time resolution, *Appl. Phys. Lett.* **102**, 051601 (2013).

- [26] T. L. Cocker, V. Jelic, M. Gupta, S. J. Molesky, J. A. J. Burgess, G. D. L. Reyes, L. V. Titova, Y. Y. Tsui, M. R. Freeman and F. A. Hegmann, An ultrafast terahertz scanning tunnelling microscope, *Nat. Photonics* **7**, 620 (2013).
- [27] S. Yoshida, Y. Aizawa, Z.-h. Wang, R. Oshima, Y. Mera, E. Matsuyama, H. Oigawa, O. Takeuchi and H. Shigekawa, Probing ultrafast spin dynamics with optical pump–probe scanning tunnelling microscopy, *Nat. Nanotechnol.* **9**, 588 (2014).
- [28] K. Yang, W. Paul, S.-H. Phark, P. Willke, Y. Bae, T. Choi, T. Esat, A. Ardavan, A. J. Heinrich and C. P. Lutz, Coherent spin manipulation of individual atoms on a surface, *Science* **366**, 509 (2019).
- [29] J. Doležal, A. Sagwal, R. C. de Campos Ferreira and M. Švec, Single-Molecule Time-Resolved Spectroscopy in a Tunable STM Nanocavity, *Nano Lett.* **24**, 1629 (2024).
- [30] P. Merino, C. Große, A. Rosławska, K. Kuhnke and K. Kern, Exciton dynamics of C60-based single-photon emitters explored by Hanbury Brown–Twiss scanning tunnelling microscopy, *Nat. Commun.* **6**, (2015).
- [31] B. McNamara and K. Wiesenfeld, Theory of stochastic resonance, *Phys. Rev. A* **39**, 4854 (1989).
- [32] R. Löfstedt and S. N. Coppersmith, Stochastic resonance: Nonperturbative calculation of power spectra and residence-time distributions, *Phys. Rev. E* **49**, 4821 (1994).
- [33] L. Gammaitoni, P. Hänggi, P. Jung and F. Marchesoni, Stochastic resonance, *Rev. Mod. Phys.* **70**, 223 (1998).
- [34] W. M. J. van Weerdenburg, H. Osterhage, R. Christianen, K. Junghans, E. Domínguez, H. J. Kappen and A. A. Khajetoorians, Stochastic Syncing in Sinusoidally Driven Atomic Orbital Memory, *ACS Nano* **18**, 4840 (2024).
- [35] T. Wagner, P. Talkner, J. C. Bayer, E. P. Rugeramigabo, P. Hänggi and R. J. Haug, Quantum stochastic resonance in an a.c.-driven single-electron quantum dot, *Nat. Phys.* **15**, 330 (2019).
- [36] R. Wiesendanger, H.-J. Güntherodt, G. Güntherodt, R. J. Gambino and R. Ruf, Observation of vacuum tunneling of spin-polarized electrons with the scanning tunneling microscope, *Phys. Rev. Lett.* **65**, 247 (1990).
- [37] S. Baumann, G. McMurtrie, M. Hänze, N. Betz, L. Arnhold, L. Malavolti and S. Loth, An Atomic-scale Vector Network Analyzer, *Small Methods* **8**, 2301526 (2024).
- [38] *See Supplemental Material at [] for the full derivation of the SRS signal, the time-dependent occupation in the case of arbitrary transition rates, a table detailing the simulation parameters used in the numerical model, a pump-probe spectrum of a single Fe atom, a differential conductance measurement of a single Fe atom using a spin-polarized tip, plots detailing deviations in the SRS signal from the lineshape of eq. 1, the error in the fitted rate, caused by*

deviations in the lineshape, details on the contribution of higher order terms to the amplitudes, displayed in Fig. 3 and an estimate of the YSR lifetime as conducted in [45].

- [39] Y. Bae, K. Yang, P. Willke, T. Choi, A. J. Heinrich and C. P. Lutz, Enhanced quantum coherence in exchange coupled spins via singlet-triplet transitions, *Sci. Adv.* **4**, eaau4159 (2018).
- [40] W. Paul, S. Baumann, C. P. Lutz and A. J. Heinrich, Generation of constant-amplitude radio-frequency sweeps at a tunnel junction for spin resonance STM, *Rev. Sci. Instrum.* **87**, 074703 (2016).
- [41] M. Hervé, M. Peter and W. Wulfhekel, High frequency transmission to a junction of a scanning tunneling microscope, *Appl. Phys. Lett.* **107**, 093101 (2015).
- [42] C. F. Hirjibehedin, C.-Y. Lin, A. F. Otte, M. Ternes, C. P. Lutz, B. A. Jones and A. J. Heinrich, Large Magnetic Anisotropy of a Single Atomic Spin Embedded in a Surface Molecular Network, *Science* **317**, 1199 (2007).
- [43] M. Ternes, Spin excitations and correlations in scanning tunneling spectroscopy, *New J. Phys.* **17**, 063016 (2015).
- [44] S. Loth, C. P. Lutz and A. J. Heinrich, Spin-polarized spin excitation spectroscopy, *New J. Phys.* **12**, 125021 (2010).
- [45] R. Rejali, D. Coffey, J. Gobeil, J. W. González, F. Delgado and A. F. Otte, Complete reversal of the atomic unquenched orbital moment by a single electron, *npj Quantum Mater.* **5**, 60 (2020).
- [46] L. U. H. Yu, Bound state in superconductors with paramagnetic impurities, *Acta Physica Sinica* **21**, 75 (1965).
- [47] H. Shiba, Classical Spins in Superconductors, *Prog. Theor. Phys.* **40**, 435 (1968).
- [48] A. I. Rusinov, Theory of gapless superconductivity in alloys containing paramagnetic impurities, *Sov. Phys. JETP* **29**, 1101 (1969).
- [49] M. Ruby, F. Pientka, Y. Peng, F. von Oppen, B. W. Heinrich and K. J. Franke, Tunneling Processes into Localized Subgap States in Superconductors, *Phys. Rev. Lett.* **115**, 087001 (2015).
- [50] H. Huang, C. Padurariu, J. Senkpiel, R. Drost, A. L. Yeyati, J. C. Cuevas, B. Kubala, J. Ankerhold, K. Kern and C. R. Ast, Tunnelling dynamics between superconducting bound states at the atomic limit, *Nat. Phys.* **16**, 1227 (2020).
- [51] U. Thupakula, V. Perrin, A. Palacio-Morales, L. Cario, M. Aprili, P. Simon and F. Masee, Coherent and Incoherent Tunneling into Yu-Shiba-Rusinov States Revealed by Atomic Scale Shot-Noise Spectroscopy, *Phys. Rev. Lett.* **128**, 247001 (2022).
- [52] J. Kondo, Resistance Minimum in Dilute Magnetic Alloys, *Prog. Theor. Phys.* **32**, 37 (1964).

- [53] D. Gatteschi, R. Sessoli and J. Villain, *Molecular Nanomagnets* (Oxford University Press, Oxford, 2006).
- [54] M. del Carmen Giménez-López, F. Moro, A. La Torre, C. J. Gómez-García, P. D. Brown, J. van Slageren and A. N. Khlobystov, Encapsulation of single-molecule magnets in carbon nanotubes, *Nat. Commun.* **2**, 407 (2011).
- [55] L. Tesi, A. Lunghi, M. Atzori, E. Lucaccini, L. Sorace, F. Totti and R. Sessoli, Giant spin–phonon bottleneck effects in evaporable vanadyl-based molecules with long spin coherence, *Dalton Trans.* **45**, 16635 (2016).
- [56] A. J. Heinrich, J. A. Gupta, C. P. Lutz and D. M. Eigler, Single-Atom Spin-Flip Spectroscopy, *Science* **306**, 466 (2004).
- [57] D. M. Eigler and E. K. Schweizer, Positioning single atoms with a scanning tunnelling microscope, *Nature* **344**, 524 (1990).
- [58] F. D. Natterer, K. Yang, W. Paul, P. Willke, T. Choi, T. Greber, A. J. Heinrich and C. P. Lutz, Reading and writing single-atom magnets, *Nature* **543**, 226 (2017).
- [59] P. Willke, T. Bilgeri, X. Zhang, Y. Wang, C. Wolf, H. Aubin, A. Heinrich and T. Choi, Coherent Spin Control of Single Molecules on a Surface, *ACS Nano* **15**, 17959 (2021).
- [60] S. Baumann, W. Paul, T. Choi, C. P. Lutz, A. Ardavan and A. J. Heinrich, Electron paramagnetic resonance of individual atoms on a surface, *Science* **350**, 417 (2015).
- [61] D. Binder, E. C. Smith and A. B. Holman, Satellite Anomalies from Galactic Cosmic Rays, *IEEE Trans. Nucl. Sci.* **22**, 2675 (1975).
- [62] L. Faoro, A. Kitaev and L. B. Ioffe, Quasiparticle Poisoning and Josephson Current Fluctuations Induced by Kondo Impurities, *Phys. Rev. Lett.* **101**, 247002 (2008).
- [63] A. Gover, A. Nause, E. Dyunin and M. Fedurin, Beating the shot-noise limit, *Nat. Phys.* **8**, 877 (2012).
- [64] B. W. Heinrich, L. Braun, J. I. Pascual and K. J. Franke, Protection of excited spin states by a superconducting energy gap, *Nat. Phys.* **9**, 765 (2013).
- [65] B. Kiraly, E. J. Knol, A. N. Rudenko, M. I. Katsnelson and A. A. Khajetoorians, Orbital memory from individual Fe atoms on black phosphorus, *Phys. Rev. Res.* **4**, 033047 (2022).
- [66] W. Paul, K. Yang, S. Baumann, N. Romming, T. Choi, C. Lutz and A. Heinrich, Control of the millisecond spin lifetime of an electrically probed atom, *Nat. Phys.* **13**, 403 (2016).

- [67] T. Sauter, W. Neuhauser, R. Blatt and P. E. Toschek, Observation of Quantum Jumps, *Phys. Rev. Lett.* **57**, 1696 (1986).
- [68] A. Singha, P. Willke, T. Bilgeri, X. Zhang, H. Brune, F. Donati, A. J. Heinrich and T. Choi, Engineering atomic-scale magnetic fields by dysprosium single atom magnets, *Nat. Commun.* **12**, 4179 (2021).
- [69] A. Spinelli, M. P. Rebergen, Otte and F. A, Atomically crafted spin lattices as model systems for quantum magnetism, *J. Phys.:Condens. Matter* **27**, 243203 (2015).
- [70] W. Steurer, J. Repp, L. Gross, I. Scivetti, M. Persson and G. Meyer, Manipulation of the Charge State of Single Au Atoms on Insulating Multilayer Films, *Phys. Rev. Lett.* **114**, 036801 (2015).
- [71] K. Vaxevani, J. Li, S. Trivini, J. Ortuzar, D. Longo, D. Wang and J. I. Pascual, Extending the Spin Excitation Lifetime of a Magnetic Molecule on a Proximitized Superconductor, *Nano Lett.* **22**, 6075 (2022).
- [72] R. Wiesendanger, Spin mapping at the nanoscale and atomic scale, *Rev. Mod. Phys.* **81**, 1495 (2009).
- [73] S. Yan, D.-J. Choi, J. A. J. Burgess, S. Rolf-Pissarczyk and S. Loth, Control of quantum magnets by atomic exchange bias, *Nat. Nanotechnol.* **10**, 40 (2014).

Figures

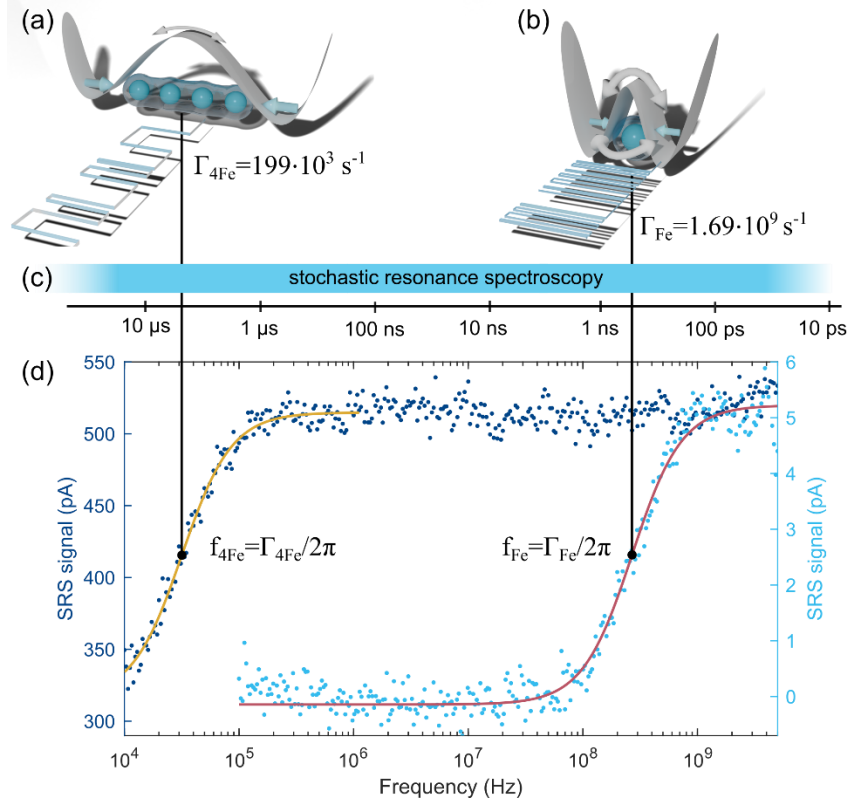


Figure 1 Stochastic resonance spectroscopy (SRS) of atomic spin-structures. (a) Sketch of the spin switching of a chain of antiferromagnetically coupled Fe atoms on Cu_2N with transition rate $\Gamma_{4\text{Fe}}$, obtained through stochastic resonance spectroscopy. The whole chain acts like a single spin with two stable states (blue arrows), separated by a barrier. Transitions (white arrow) overcome this barrier sporadically and result in slow stochastic switching (blue ribbon). (b) Sketch of the switching of a single Fe atom on Cu_2N with transition rate Γ_{Fe} . Elements in the sketch are analogous to (a). The reduced barrier height and significant quantum tunneling of magnetization transitions gives rise to a faster transition rate (illustrated by bold white arrows). (c) Illustration of the time scales accessible to measurements using SRS (blue ribbon). Lifetimes of the two structures in (a) and (b) are marked with black lines. (d) Stochastic resonance spectroscopy of the structures in (a) and (b), showing the tunnel current as function of microwave frequency. The measurement on the four-atom chain (dark blue axis) shows a step in current of 199 ± 2 pA amplitude, centered at $f_{4\text{Fe}} = 31.7$ kHz (marked by black dot). The measurement on the single atom (light blue axis) shows a step in current of 5.37 ± 0.05 pA amplitude, centered at $f_{\text{Fe}} = 269$ MHz (marked by black dot). Fits using eq. 1 yield transition rates of $\Gamma_{4\text{Fe}} = 199 \pm 5 \cdot 10^3/\text{s}$ (yellow) and $\Gamma_{\text{Fe}} = 1.69 \pm 0.05 \cdot 10^9/\text{s}$ (red). The measurement on the four-atom chain was performed with a microwave amplitude of $V_{ac} = 1.4$ mV, the one on the single atom with a microwave amplitude of $V_{ac} = 2.8$ mV. Both measurements use an offset voltage of $V_{dc} = 4$ mV, a tunnel junction setpoint 4 nA at 10 mV. Magnetic field 2 T, applied parallel to the easy magnetic axis of the spins. Temperature 2.4 K.

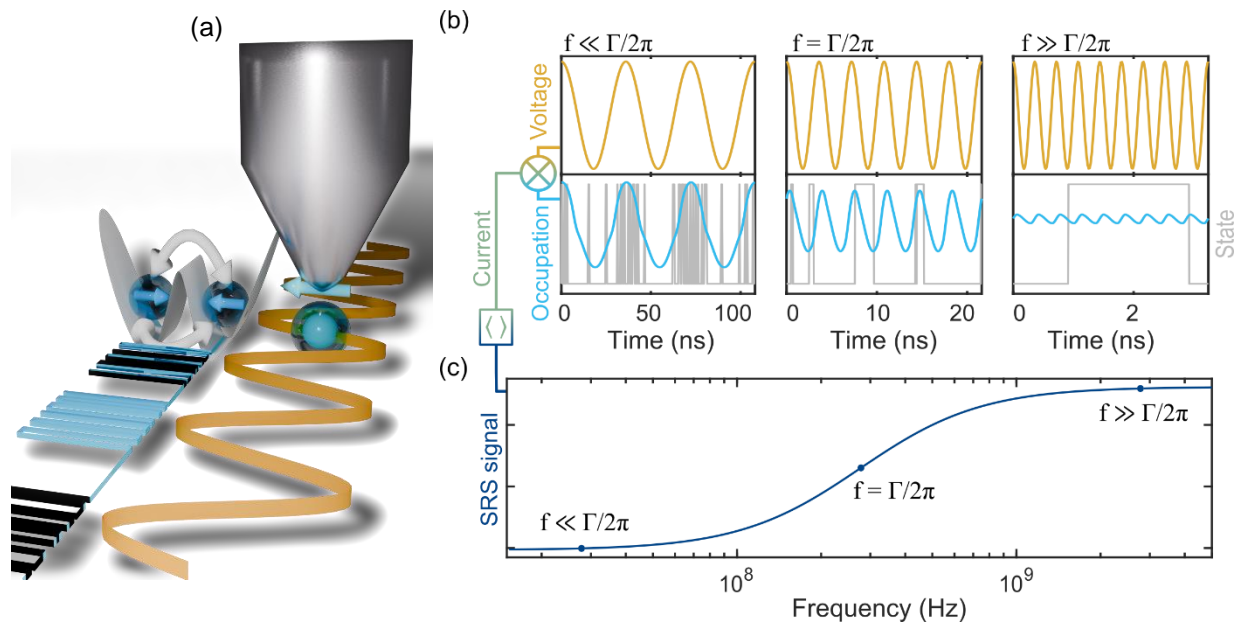


Figure 2 Detection mechanism of stochastic resonance spectroscopy. (a) Sketch of the effect of the microwave drive (yellow ribbon) on the spin switching (blue ribbon) at microwave frequencies $f \ll \Gamma/2\pi$. The drive, applied to the atom (light blue sphere) using a spin-polarized tip (indicated by light blue arrow), facilitates transitions (white arrows) between the spin states (blue arrows), that are separated by an energy barrier. (b) The voltage of the microwave modulation (yellow) mixes with the spin system's occupation probability (blue) and representative state occupation (grey). The time-dependent occupation probability changes with microwave frequency f (left to right: 28 MHz: $f \ll \Gamma/2\pi$, 278 MHz: $f = \Gamma/2\pi$ and 2.7 GHz: $f \gg \Gamma/2\pi$). (c) Resulting SRS signal (see eq. 1 in the main text), given by low-passed detection of the homodyne component of the oscillating tunnel current. All figures are based on physical rates of an Fe atom on Cu_2N .

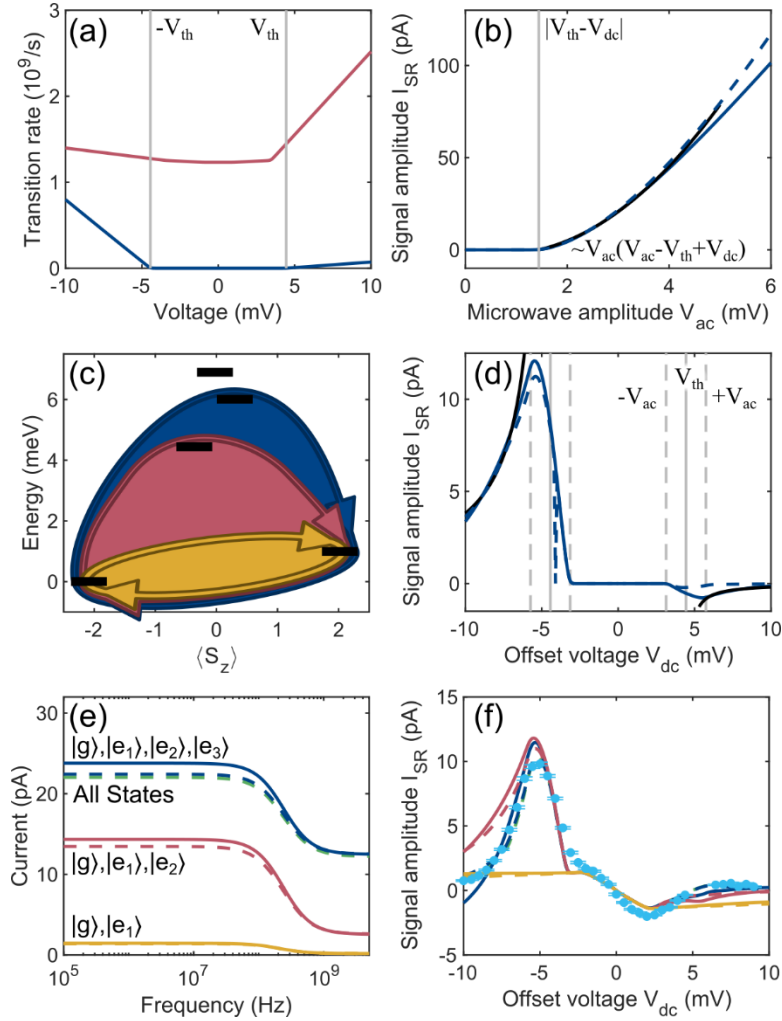


Figure 3 Factors determining the amplitude of the SRS signal. (a) Excitation (blue) and relaxation rates (red) of a two-state system with a threshold (gray) at $V_{th} = \pm 4.4$ meV. (b) SRS signal amplitude I_{SR} (blue) as a function of microwave amplitude V_{ac} for the two-state system of (a) with fit (black) according to the lowest order homodyne signal $\sim V_{ac}(V_{ac} - V_{th} + V_{dc})$. The gray line marks the minimal V_{ac} , where the voltage reaches the threshold V_{th} for $V_{dc} = -3$ mV. The dashed line shows the behavior of the full five-state system described in c. (c) Energy of the five spin states of an Fe atom on $Cu_2N/Cu(100)$ labeled $|g\rangle$ and $|e_1\rangle$ to $|e_4\rangle$ as function of magnetic moment $\langle S_z \rangle$. The colored areas encircle the states used in the simulations in (e,f) and illustrate relevant transitions. (d) SRS signal amplitude I_{SR} (blue) as a function of offset voltage V_{dc} for $V_{ac} = 1.3$ mV with fit (black) according to the lowest order homodyne signal ($j = 1$) for the two-state system (blue line) and the five-state calculation. (e) Changes in SRS signal upon including different sets of states $|g\rangle, |e_1\rangle$ to $|e_4\rangle$ in the calculation of the spin system of (c). (f) Measured and calculated SRS signal amplitude for a single Fe atom on Cu_2N ($V_{ac} = 1.3$ mV, $T = 0.5$ K, $V_{set} = 10$ mV, $I_{set} = 1$ nA, $B = 2$ T). Rates are obtained from scattering theory (parameters: Supplemental Material, table 1 [38]). All SRS signal amplitudes I_{SR} are obtained by numerical simulation (dashed lines) and analytical calculations including terms with orders up to $j = 2$ (solid lines).

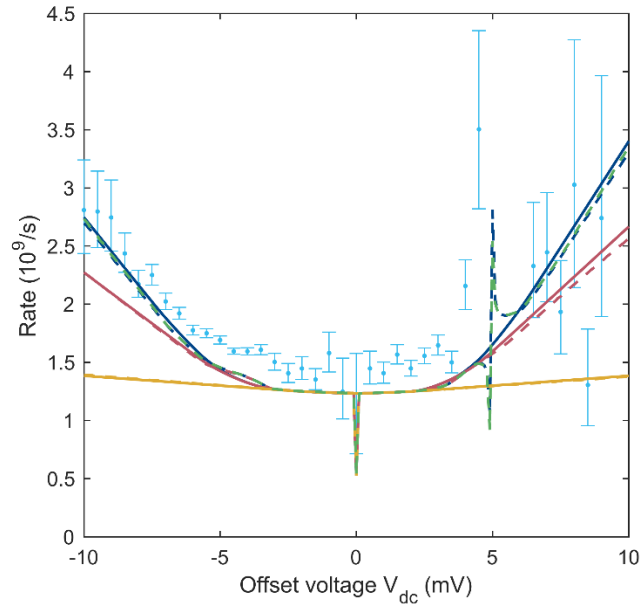


Figure 4 Driven dynamics of a single Fe atom on Cu₂N. The measured rates (light blue dots) are obtained by fitting SRS measurements using eq. 1. Error bars indicate one standard deviation from the fitted value. The simulations using an effective two-state model (solid lines) and the full five-state model (dashed lines) use parameters in Supplemental Material, table 1 [38], and include different sets of states (yellow: $|g\rangle, |e_1\rangle$, red: $|g\rangle, |e_1\rangle, |e_2\rangle$, blue: $|g\rangle, |e_1\rangle, |e_2\rangle, |e_3\rangle$, green: all states). Colors are matched with Fig. 3e,f. ($V_{ac} = 1.3$ mV, $T = 0.5$ K, $V_{set} = 10$ mV, $I_{set} = 1$ nA, $B = 2$ T).

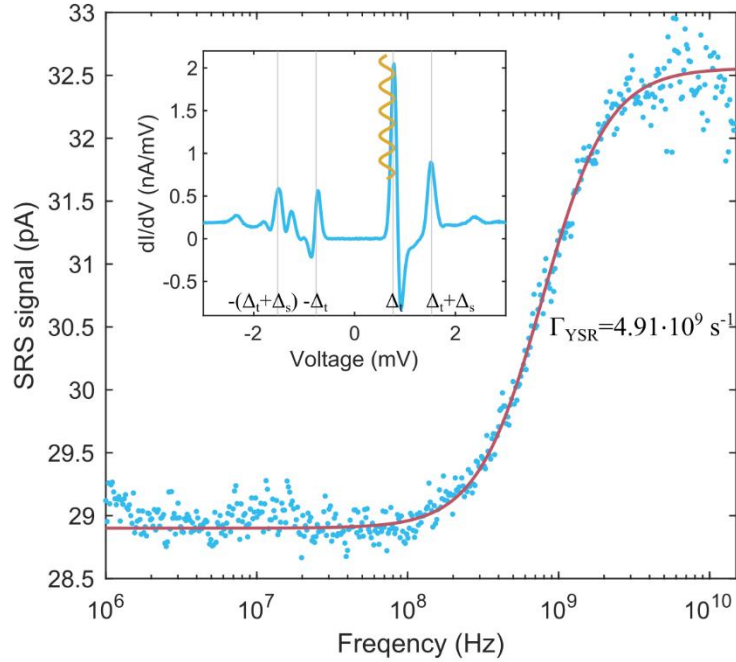


Figure 5 Stochastic resonance spectroscopy (SRS) of a Yu-Shiba-Rusinov state. The SRS signal recorded with a superconducting tip on a Fe atom on V(100)(1×5) (blue dots) shows a step in current of -3.66 ± 0.02 pA amplitude, centered at $f_{YSR} = 0.780$ GHz. Fits using eq. 1 of the main text yield a transition rate of $\Gamma_{YSR} = (4.91 \pm 0.06) \cdot 10^9/s$ (red curve). The measurement used a microwave amplitude of $V_{ac} = 140 \mu V$ (yellow line in inset) and an offset voltage of $V_{ac} = 640 \mu V$. Tunnel junction setpoint 1 nA at 10 mV. Temperature 50 mK. Inset: Differential conductivity measurement (dI/dV) of the YSR state. Excitation thresholds of the tip Δ_t and the sample Δ_s are marked in gray.

Supplemental Material:

Stochastic Resonance Spectroscopy: Characterizing Fast Dynamics with Slow Measurements

Nicolaj Betz^{1,2}, Gregory McMurtrie¹, Max Hänze^{1,3}, Vivek Krishnakumar Rajathilakam¹, Laëtitia Farinacci^{1,4}, Susan N. Coppersmith⁵, Susanne Baumann¹ and Sebastian Loth^{1,2,3}

¹ University of Stuttgart, Institute for Functional Matter and Quantum Technologies, 70569 Stuttgart, Germany.

² Center for Integrated Quantum Science and Technology (IQST), University of Stuttgart, 70569 Stuttgart, Germany.

³ Max Planck Institute for Solid State Research, 70569 Stuttgart, Germany.

⁴ Carl-Zeiss-Stiftung Center for Quantum Photonics Jena – Stuttgart – Ulm, Germany.

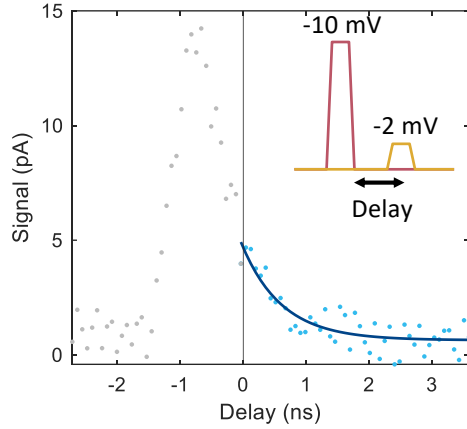
⁵ School of Physics, University of New South Wales, Sydney, Australia.

Contents:

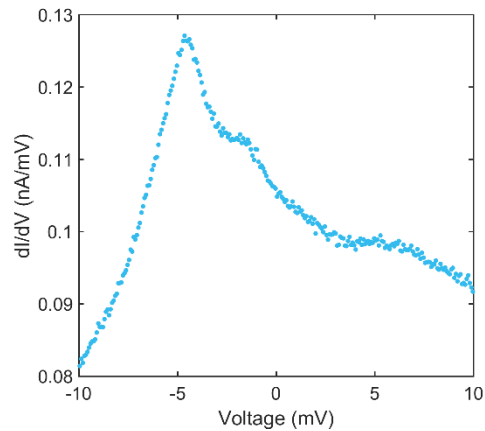
Supplementary figures S1 – S7s

Supplementary table S1

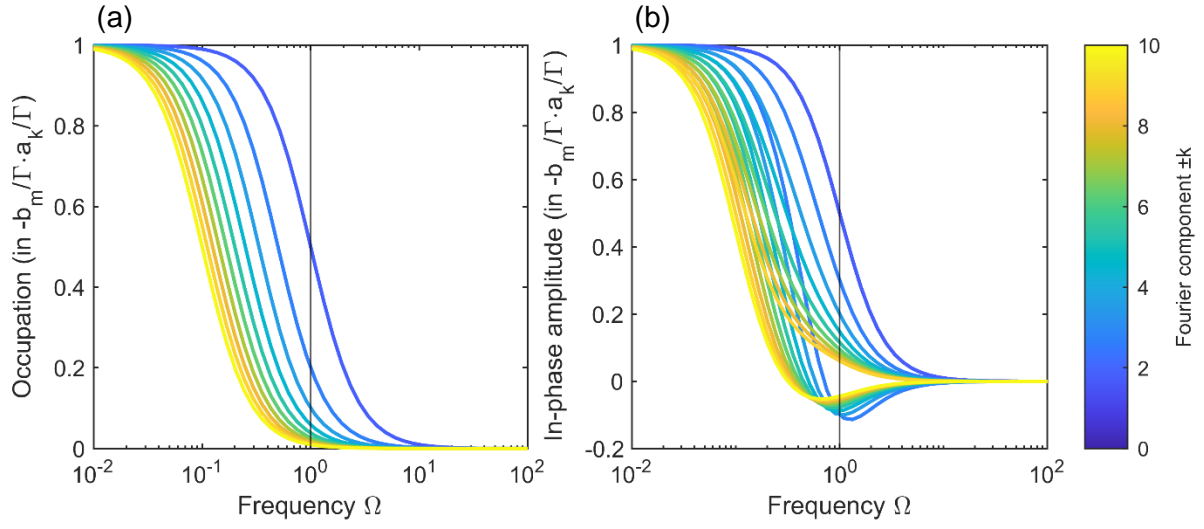
S1: Solution to the analytic two-state model	9
S1.1 Calculation of state occupation with constant Γ	9
S1.2 Calculation of state occupation with time-dependent $\Gamma(t)$	10
S2 Occupation in the high and low frequency limit	13
S2.1 Occupation at $\Omega \gg 1$	13
S2.2 Occupation at $\Omega \ll 1$	13
S3 Numerical simulation of dynamics	14
S4 Methods	15
S4.1 Experimental setup	15
S4.2 Sample preparation	15
S4.3 Atom manipulation	15



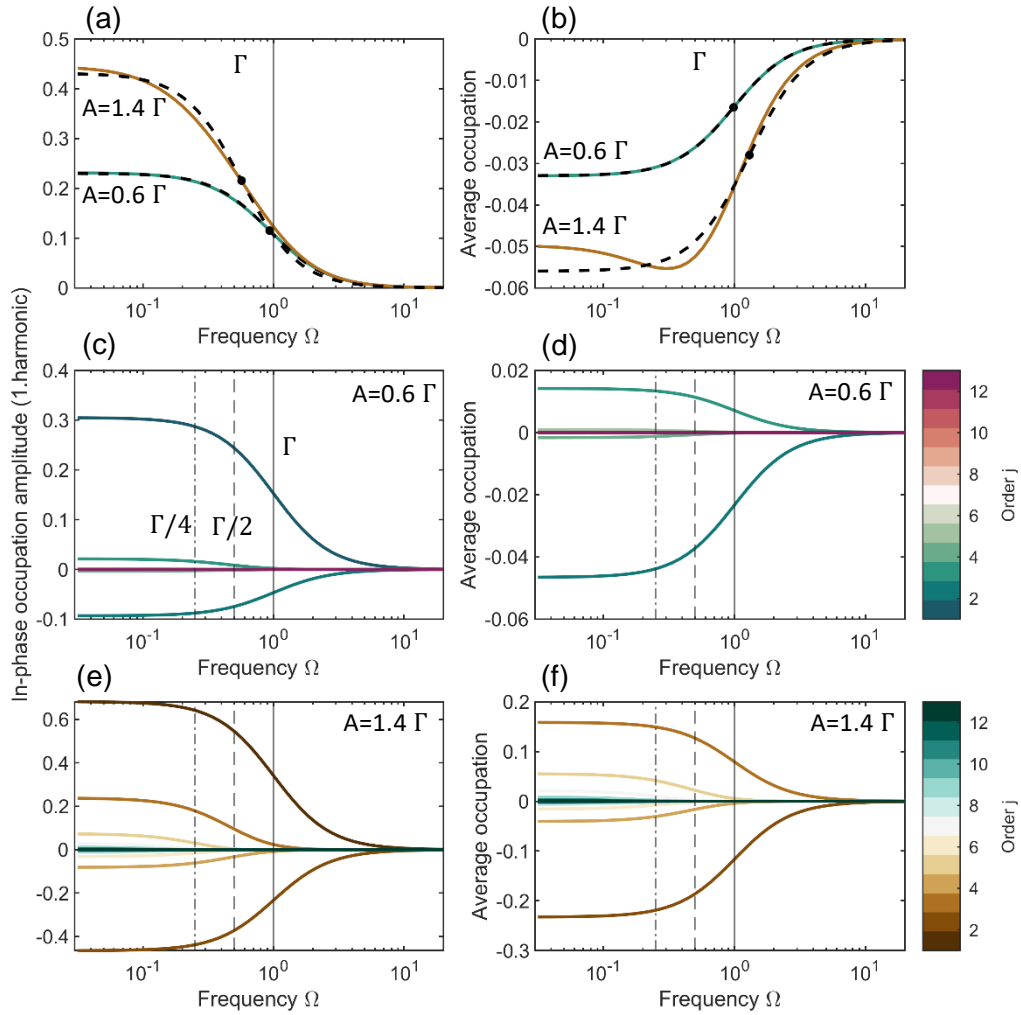
Supplementary Figure S1 Electronic pump-probe measurement of a single Fe atom on Cu₂N. In this experiment, two 429 ps voltage pulses (pump: -10 mV, probe: -2 mV) with rise times of 154 ps and varying delay are applied to the tunnel junction. The resulting current signal decays as the excited spin population relaxes [24]. The exponential fit to the signal decay (dark blue) results in a lifetime of $T_1 = 0.6 \pm 0.1$ ns. The spin-polarized tip in this measurement is the same as the tip in Figure 1 of the main text. The measurement has been performed using an active state setpoint voltage and current of $V_{\text{set}} = 10$ mV, $I_{\text{set}} = 5$ nA, in a magnetic field of $B = 2$ T and at a temperature $T = 2.4$ K.



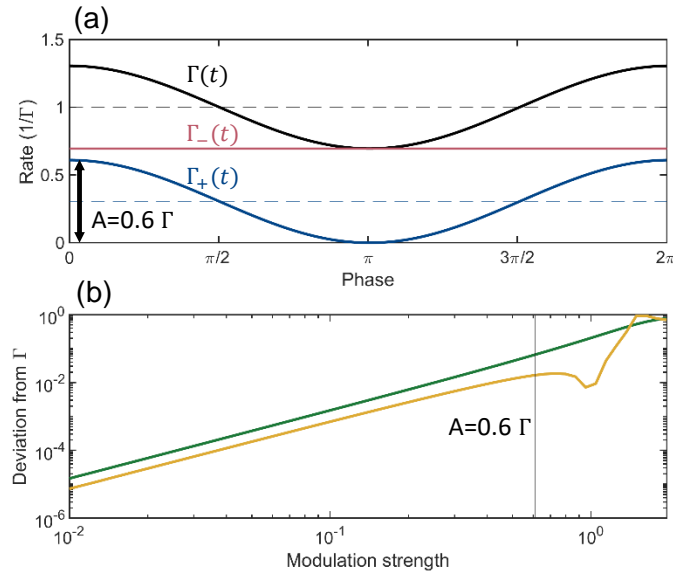
Supplementary Figure S2 Differential conductivity dI/dV of a single Fe atom on Cu₂N, measured with a spin-polarized tip. The spin-polarized tip in this measurement is the same as the tip in Figure 1 of the main text. The measurement has been performed using an active state setpoint voltage and current of $V_{\text{set}} = 10$ mV, $I_{\text{set}} = 1$ nA, in a magnetic field of $B = 2$ T and at a temperature $T = 2.4$ K.



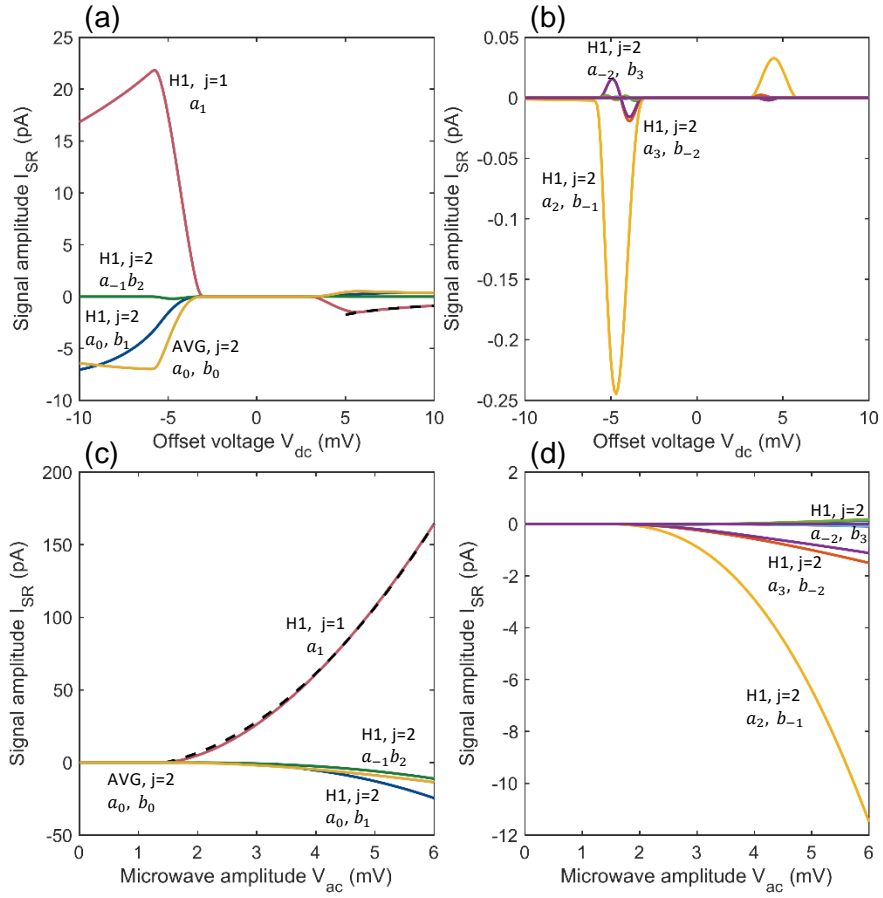
Supplementary Figure S3 Frequency-dependence of 2nd order terms The figure shows the $j = 2$ -terms of eq. [19] (see section S1.2 in supplemental material) that contribute to the average occupation ($m + k = 0$) (a) and the in-phase occupation amplitude oscillating at ω , ($m + k = \pm 1$) (b). Each curve is normalized by the respective Fourier components $-b_m/\Gamma$ a_k/Γ , encoded in the color scale.



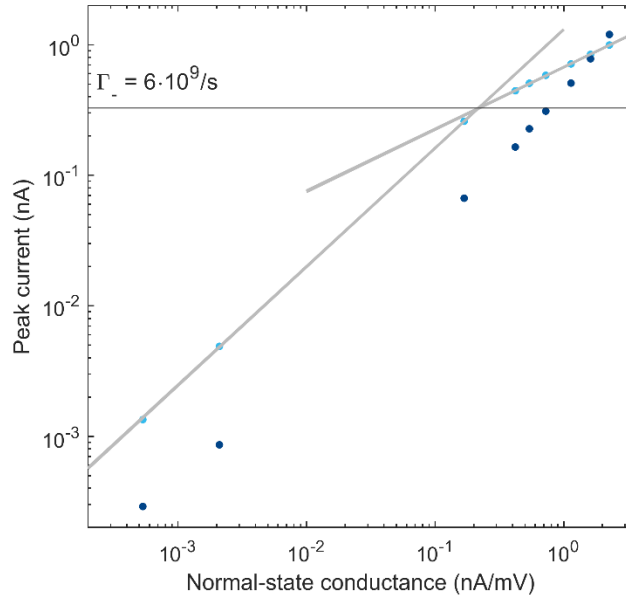
Supplementary Figure S4 Contribution of different orders j to the average occupation and the in-phase occupation amplitude, oscillating at ω . (a, b) Total in-phase occupation amplitude and average occupation at modulation strengths $A = 0.6 \Gamma$ (purple) and 1.4Γ (yellow), plotted together with fits, using eq. 1 of the main text (dashed lines). The extracted rates are marked with a dot. The rates due to a modulation strength of $A = 0.6 \Gamma$ are shown in supplementary Fig. S5a, while those for the larger modulation amplitude would increase accordingly. (c, e) Contribution of terms of order j up to $j_{\max} = 13$ to the in-phase occupation amplitude for the two different modulation strength $A = 0.6 \Gamma$ (c) and 1.4Γ (e). (d, f) Contribution of terms of order j up to $j_{\max} = 13$ to the average occupation for the respective modulation strength. Respective orders are displayed according to the color scale on the right. Gray lines mark Γ (solid lines), $\Gamma/2$ (dashed lines) and $\Gamma/4$ (dashed-dotted lines). Overall, this figure shows how larger modulation strengths promote higher order contributions that shift the total signal toward lower frequencies and cause distortions in the measured SRS signal.



Supplementary Figure S5 Effect of large variations in the total transition rate (a) Excitation, relaxation and total rates for modulation strength of $A = 0.6\Gamma$ in units of Γ . The excitation rate $\Gamma_+(t) = \frac{A}{2}(1 + \cos(\omega t))$ (blue) modulates sinusoidally from 0 to A while the relaxation rate $\Gamma_- = \Gamma - \langle \Gamma_+ \rangle$ (red) is constant. The resulting total rate $\Gamma(t) = \Gamma_+(t) + \Gamma_-$ is displayed in black. Dashed lines mark the average of their respective rates. (b) Such large modulation strength lead to deviations in the extracted rate, these deviation from the actual rate Γ as displayed here: increasing modulation strength leads to larger deviations from the rate, typically shifting the extracted rate to smaller Γ (as shown in supplementary Fig. S6a). The plotted deviations are obtained by fitting the theoretical signal, due to the average occupation probability (yellow) and due to homodyne mixing (green), with eq. 1 of the main text. These deviations can be understood as the error in Γ when using eq. 1, induced by higher-order contributions. The theoretical signal is calculated including all contributions up to order $j = 13$. Modulation strengths up to $A = 0.6\Gamma$ (gray line) result in deviations of less than 5% of the actual rate.



Supplementary Figure S6 Contributions to the SRS signal amplitude in Fig. 3b and 3d of the main text. (a,b) Contributions to the SRS signal amplitude as a function of offset voltage V_{dc} (c,d) Contributions to the SRS signal amplitude as a function of microwave drive amplitude V_{ac} . The main deviations from the lowest order behavior (H1, $j=1$) appear around the excitation threshold. The curves are denoted by their order j , the type of their contribution (homodyne signal H1 or average occupation signal AVG) and by their respective Fourier components (a_k, b_m) in the plots. Contributions with $a_{|k|\geq 2}$, that distort the SRS lineshape are displayed in (b,d). Those that do not distort the SRS lineshape are displayed in (a,c). All contributions are calculated according to the analytical theory and use the rates obtained from scattering theory.



Supplementary Figure S7 Maximum tunneling current through a Yu-Shiba-Rusinov state on V(100). The tunneling current through the Yu-Shiba-Rusinov state of an individual Fe atom on V(100) as used in Figure 5 of the main text is displayed as a function of junction conductance. At positive voltages (light blue data points) the current displays a linear and a sub-linear regime, fitted individually using a power law (grey lines). While the current at negative voltages (dark blue) does not display a transition between linear and sub-linear regimes. For positive voltages, the current at the intersection between the linear and sub-linear regime (black line) estimates the relaxation rate of the system to $\Gamma_- \approx 6 \cdot 10^9 /s$. The normal-state conductance is obtained through the current at 3 mV. All measurements are taken at $T=50$ mK.

Parameter	Values
Total spin S	2
Spin-polarization tip η	0.86
Potential scattering u	0.76
g-factor	2.15
Magnetic field B	2 T
Uniaxial anisotropy D	-1.557 meV
Transversal anisotropy E	0.248 meV
'Sample-sample' conductivity C_{SS}	7.2 μS
'Sample-tip conductivity C_{ST}	0.500 μS
Linearized conductivity difference $\Delta\sigma$	-0.26 μS

Supplementary Table 1 Simulation parameters. The simulations follow references [44] and [43], and are adjusted for a single Fe atom on Cu₂N. The displayed parameters are those used to simulate the SRS measurements on the single Fe atom in Figures 3 and 4 of the main text. Parameters were obtained by fitting the signal of the numerically evolved dynamics to the measurement in Fig. 1 and adjusting parameters to match the experimental data in Figures 3f and 4. The linearized conductivity difference is obtained by calculating state-dependent tunneling rates in the relevant voltage range and calculating the average conductivity of each state.

S1: Solution to the analytic two-state model

A two-state Markov-chain can be described by the following rate equation:

$$\frac{dn}{dt} = \Gamma_+(t) - (\Gamma_+(t) + \Gamma_-(t)) \cdot n \quad [1]$$

where n is the occupation probability of one of the states, and Γ_+ (Γ_-) the transition rate into (from) that state.

Starting from this rate description, it is convenient to use a rescaled time $\tau = \Gamma t$, with Γ being average of the total rate: $\Gamma = \langle \Gamma(t) \rangle = \langle \Gamma_+(t) + \Gamma_-(t) \rangle$. Written with this rescaled time, the rate equation becomes:

$$\frac{dn}{d\tau} = \frac{\Gamma_+(\tau)}{\Gamma} - \frac{\Gamma(\tau)}{\Gamma} n. \quad [2]$$

In stochastic resonance spectroscopy (SRS), we modulate the rates with a periodic drive, which makes the rates also periodic with the driving frequency ω . We again use a rescaled frequency $\Omega = \omega/\Gamma$.

The linear, first order differential equation, of eq. [2] with periodic parameters can be solved using [29,28]

$$n(\tau) = \frac{1}{1 - e^{-2\pi/\Omega}} \int_0^{2\pi/\Omega} \frac{\Gamma_+(\tau - \tau')}{\Gamma} e^{-\tau'} h(\tau - \tau', \tau) d\tau', \quad [3]$$

$$h(\tau - \tau', \tau) = e^{-\int_{\tau-\tau'}^{\tau} \frac{\Gamma(\tau'')}{\Gamma} - 1 d\tau''}. \quad [4]$$

In the following, we discuss the solution of the differential equation first for the case of constant Γ , and then we discuss the solution for time-dependent rates $\Gamma(t)$.

S1.1 Calculation of state occupation with constant Γ

As in the main text, we start with the case where $\Gamma(t) = \Gamma = \text{const}$. In this case, the h -term in eq. [4] becomes

$$h(\tau - \tau', \tau) = e^{-\int_{\tau-\tau'}^{\tau} 1 - 1 d\tau''} = 1 \quad [5]$$

and the occupation probability simplifies to

$$n(\tau) = \frac{1}{1 - e^{-2\pi/\Omega}} \sum_k A_k \int_0^{2\pi/\Omega} e^{ik\Omega(\tau-\tau')} e^{-\tau'} d\tau' \quad [6]$$

where the parameters A_k stem from the Fourier series of the rate

$$\frac{\Gamma_+(\tau)}{\Gamma} = \sum_k \frac{a_k}{\Gamma} e^{ik\omega\tau} = \sum_k A_k e^{ik\Omega\tau}.$$

[7]

Note that positive rates imply that $a_m \leq a_0 \leq \Gamma$, i.e. $A_k \leq 1$.

In this form, the integral in eq. [6] can be evaluated directly, giving:

$$\int_0^{2\pi/\Omega} e^{-(ik\Omega+1)\tau'} d\tau' = \frac{1}{-(ik\Omega+1)} [e^{-(ik\Omega+1)\tau'}]_0^{2\pi/\Omega} = \frac{1}{-(ik\Omega+1)} \left(e^{-(ik\Omega+1)\frac{2\pi}{\Omega}} - 1 \right)$$

[8]

and thus the occupation reduces to

$$n(\tau) = \sum_k A_k \frac{1}{ik\Omega+1} e^{ik\Omega\tau} = \sum_k \frac{a_k}{\Gamma} \frac{1-ik\Omega}{k^2\Omega^2+1} e^{ik\Omega\tau}.$$

[9]

As described in the main text (section III), the experimental signal consists of contributions proportional to the average occupation probability and the in-phase component of the occupation probability, oscillating at the driving frequency. In the case of constant Γ , the average occupation is the term with $k = 0$ and constant with frequency. The components oscillating at the driving frequency are given by the $k = \pm 1$ terms. The homodyne detection mixes down their in-phase components, i.e. the real part of the $k = \pm 1$ terms. The signal thus becomes

$$I^{\Gamma=const.} = \Delta\sigma V_{ac} \frac{a_{\pm 1}}{\Gamma} \frac{1}{\Omega^2+1} + I_{rec},$$

[10]

where $\Delta\sigma$ is the conductivity difference between the two states, V_{ac} is the amplitude of the voltage modulation and I_{rec} are all frequency-independent contributions to the current. Experimentally, this frequency-independent offset also includes a signal due to rectification of the voltage modulation on a non-linear tunneling characteristic, e.g. caused by the inelastic scattering of the tunneling electrons. Such frequency-independent signals are commonly used to characterize the transmission of the experimental setup [37].

S1.2 Calculation of state occupation with time-dependent $\Gamma(t)$

The derivation in S1.1 outlines the derivation of the occupation probability when $\Gamma(t) = \Gamma = const.$ We now consider the general case in which the time-dependence of $\Gamma(t)$ is taken into account.

We start by writing the total rate $\Gamma(t)$ in its Fourier series

$$\frac{\Gamma(\tau)}{\Gamma} = \sum_k \frac{b_k}{\Gamma} e^{ik\omega\tau} = 1 + \sum_{k \neq 0} B_k e^{ik\Omega\tau}.$$

[11]

Note that positive rates imply that $b_m \leq \Gamma$ (i.e. $B_k \leq 1$), since here $b_0 = \Gamma$.

This enables us to evaluate the integral in the h -term, and gives:

$$h(\tau - \tau', \tau) = e^{-\int_{\tau-\tau'}^{\tau} \sum_{k \neq 0} B_k e^{ik\Omega\tau'} d\tau''} = e^{-\sum_{k \neq 0} \frac{B_k}{ik\Omega} (e^{ik\Omega\tau} - e^{ik\Omega(\tau-\tau')})}.$$

[12]

While this is an explicit solution of the h -term, the nested exponentials still prevent the straight-forward calculation of the occupation. Thus, we now expand the outer exponential as:

$$h(\tau - \tau', \tau) = \sum_{j=1} \frac{1}{(j-1)!} \left(\frac{1}{i\Omega}\right)^{j-1} \left(-\sum_{k \neq 0} \frac{B_k}{k} e^{ik\Omega\tau} (1 - e^{-ik\Omega\tau'})\right)^{j-1}. \quad [13]$$

This form shows that, already within the h -term, various harmonics of the rate $\Gamma(t)$ mix. This takes place in terms with $j \geq 3$. For instance, the term with order $j = 3$ describes mixing between any $j - 1 = 2$ harmonics of the drive.

Since we treat real periodic signals, the sum over k converges and can in practice be truncated to a finite order N . This allows us to expand the multinomial in the following way:

$$h(\tau - \tau', \tau) = \sum_{j=1} \frac{1}{(j-1)!} \left(\frac{1}{i\Omega}\right)^{j-1} \sum_{|\mathbf{L}|=j-1} \binom{j-1}{\mathbf{L}} \prod_{n=1}^N \left(\frac{-B_{k_n}}{k_n} e^{ik_n\Omega} (1 - e^{-ik_n\Omega\tau'})\right)^{L_n}. \quad [14]$$

Here, we adopt a notation with multi-indices $\mathbf{L} = (L_1, L_2, \dots, L_N)$ and $\mathbf{k} = (k_1, k_2, \dots, k_N)$, where the multinomial coefficients are $\binom{j}{\mathbf{L}} = \frac{j!}{L_1! L_2! \dots L_{j-1}!}$ and $|\mathbf{L}| = \sum_{n=1}^N L_n$.

Additionally, rearranging the multiplication and introducing the integer $S(\mathbf{L}, \mathbf{k}) = \sum_n L_n k_n$ yields

$$h(\tau - \tau', \tau) = \sum_{j=1} \frac{1}{(j-1)!} \sum_{|\mathbf{L}|=j-1} \binom{j-1}{\mathbf{L}} e^{iS(\mathbf{L}, \mathbf{k})\Omega\tau} \left(\frac{1}{i\Omega}\right)^{j-1} \prod_n \left(\frac{-B_{k_n}}{k_n}\right)^{L_n} (1 - e^{-ik_n\Omega\tau'})^{L_n} \quad [15]$$

The last step is to expand the terms with τ'

$$\begin{aligned} & h(\tau - \tau', \tau) \\ &= \sum_{j=1} \frac{1}{(j-1)!} \sum_{|\mathbf{L}|=j-1} \binom{j-1}{\mathbf{L}} e^{iS(\mathbf{L}, \mathbf{k})\Omega\tau} \left(\frac{1}{i\Omega}\right)^{j-1} \left(\prod_n \left(\frac{-B_{k_n}}{k_n}\right)^{L_n}\right) \sum_{\mathbf{l} \leq \mathbf{L}} \binom{\mathbf{L}}{\mathbf{l}} (-1)^{|\mathbf{l}|} e^{-iS(\mathbf{l}, \mathbf{k})\Omega\tau'}, \end{aligned} \quad [16]$$

which introduces another multi-index $\mathbf{l} = (l_1, l_2, \dots, l_N)$, where the sum over $\mathbf{l} \leq \mathbf{L}$ covers all $l_n \leq L_n$ and the binomial coefficients are $\binom{\mathbf{L}}{\mathbf{l}} = \binom{L_1}{l_1} \cdot \binom{L_2}{l_2} \cdot \dots \cdot \binom{L_N}{l_N}$.

It is now possible to evaluate the integral in eq. [3] by using the Fourier expansion of the excitation rate from eq. [7] and the h -term from eq. [16]. The integral over τ' gives rise to:

$$\int_0^{2\pi/\Omega} e^{-(ik\Omega + 1 + iS(\mathbf{l}, \mathbf{m})\Omega)\tau'} d\tau' = \frac{1}{i(k + S(\mathbf{l}, \mathbf{m}))\Omega + 1} \left(1 - e^{-i(k + S(\mathbf{l}, \mathbf{m}))\Omega + 1} \frac{2\pi}{\Omega}\right). \quad [17]$$

As a result, harmonics stemming both from the h -term and the excitation rate are mixed giving rise to the following expression for the occupation probability:

$$n(\tau) = \sum_k A_k \sum_{j=1} \frac{1}{(j-1)!} \sum_{|\mathbf{L}|=j-1} \binom{j-1}{\mathbf{L}} \left(\prod_n \left(\frac{-B_{m_n}}{m_n}\right)^{L_n}\right) e^{i(k + S(\mathbf{L}, \mathbf{m}))\Omega\tau} \left(\frac{1}{i\Omega}\right)^{j-1} \sum_{\mathbf{l} \leq \mathbf{L}} \binom{\mathbf{L}}{\mathbf{l}} \frac{(-1)^{|\mathbf{l}|}}{i(k + S(\mathbf{l}, \mathbf{m}))\Omega + 1}$$

$$= \sum_k \sum_{j=1} \sum_{|\mathbf{L}|=j-1} \binom{j-1}{\mathbf{L}} \frac{a_k}{\Gamma} \prod_n \left(\frac{-b_{m_n}}{\Gamma} \right)^{L_n} e^{i(k+S(\mathbf{L}, \mathbf{m}))\Omega\Gamma t} \frac{1}{(j-1)! i^{j-1} \Omega^{j-1} \prod_n m_n^{L_n}} \sum_{\mathbf{l} \leq \mathbf{L}} \binom{\mathbf{L}}{\mathbf{l}} \frac{(-1)^{|\mathbf{l}|}}{i(k+S(\mathbf{l}, \mathbf{m}))\Omega + 1} \quad [18]$$

This expression is rather complex as it describes the very general case of arbitrary $\Gamma(t)$. In practice, the rates are often dominated by a finite order in the mixing of harmonics of the drive and all harmonics are smaller or equal to the average of the rate ($b_m, a_k \leq \Gamma$), i.e. the series converges. It is therefore meaningful to treat the sum over j that represents the number of mixing Fourier components as a series expansion of the occupation and neglect high orders of j .

Explicitly, the terms up to $j = 2$ are:

$$n(t) = \underbrace{\sum_k \frac{a_k}{\Gamma} \frac{1 - ik\Omega}{k^2\Omega^2 + 1} e^{ik\Omega\Gamma t}}_{j=1} + \underbrace{\sum_k \sum_{m \neq 0} \frac{a_k - b_m}{\Gamma} \frac{1}{m} \left[\frac{(m+k) + \frac{i}{\Omega}}{(m+k)^2\Omega^2 + 1} - \frac{k + i/\Omega}{k^2\Omega^2 + 1} \right]}_{j=2} e^{i(k+m)\Omega\Gamma t} + \underbrace{O\left(\frac{a_k}{\Gamma} \left(\frac{b_m}{\Gamma}\right)^2\right)}_{j>2}$$

[19]

S2 Occupation in the high and low frequency limit

A physical understanding of the dynamics at play can be gained by looking at the occupation probability in the high and low frequency limits (see also Figure 2 of the main text).

S2.1 Occupation at $\Omega \gg 1$

At high frequencies, we have $\frac{1}{\Omega^{j-1}} \rightarrow 0$ for $j > 1$. The only term remaining in eq. [18] is thus the one with $j = 1$ (i.e. the first sum in eq. [19]). As a result, Fourier components with $k \neq 0$ oscillate at $k\Omega$ averaging to 0 and the only component in the occupation remaining is that with $k = 0$ leading to:

$$n^{\Omega \gg 1} = \frac{a_0}{\Gamma} = \frac{\langle \Gamma_+(t) \rangle}{\langle \Gamma(t) \rangle}. \quad [20]$$

At high frequencies, the occupation probability thus only depends on the average of the rates: their modulation over time is too fast for the system to react.

S2.2 Occupation at $\Omega \ll 1$

For small frequencies, we find numerically that the terms in eq. [18] also simplify. More precisely, we verified that up to $j = 13$ (covering most physical scenarios) the following term:

$$\frac{1}{(j-1)! i^{j-1} \Omega^{j-1} \prod_n m_n^{L_n}} \sum_{l \leq L} \binom{L}{l} \frac{(-1)^{|l|}}{i(k + S(\mathbf{l}, \mathbf{m}))\Omega + 1} \quad [21]$$

tends to unity. In the case of $j = 2$, this is shown in supplementary figure S3: there we display the first 10 k -terms of the $j = 2$ sum of eq. [18]. Assuming that this finding applies for all j , the occupation becomes

$$n^{\Omega \ll 1}(\tau) = \sum_k \frac{a_k}{\Gamma} e^{ik\Omega\tau} \sum_{j=1} \sum_{|L|=j} \binom{j-1}{L} \prod_n (-B_{m_n})^{L_n} e^{iS(L, \mathbf{m})\Omega\tau}, \quad [22]$$

where we can identify the multinomial expansion and get

$$n^{\Omega \ll 1}(\tau) = \sum_k \frac{a_k}{\Gamma} e^{ik\Omega\tau} \sum_{j=1} \left(\sum_{m \neq 0} -B_m e^{im\Omega\tau} \right)^{j-1}. \quad [23]$$

Here, the sum over j is the geometric series of the Fourier series of the rate and we have

$$n^{\Omega \ll 1}(\tau) = \frac{\sum_k \frac{a_k}{\Gamma} e^{ik\Omega\tau}}{1 - \sum_{m \neq 0} -b_m / \Gamma e^{im\Omega\tau}} = \frac{\Gamma_+(t)}{\Gamma(t)}. \quad [24]$$

The occupation is therefore the ratio of the excitation rate $\Gamma_+(t)$ to the total rate $\Gamma(t)$. This result is identical with the steady state solution of the rate equation:

$$\frac{dn}{dt} = 0 = \Gamma_+(t) - \Gamma(t)n. \quad [25]$$

S3 Numerical simulation of dynamics

Our analytical model is derived for the special case of a two-level system. To assess how well it fares for multi-level systems, we compare it to numerical simulations for the Fe atom as shown in Figures 3 and 4 of the main text. In our numerical simulation, we consider voltage-dependent transition rates $\Gamma_{fi}(V)$ from any initial state i to any final state f of the physical n -state system: $\Gamma_{fi}(t, \omega) = \Gamma_{fi}(V_{dc} + V_{ac} \cos(\omega t))$. The voltage-dependent scattering rates are derived according to the scattering theory described in references [44] and [43]. The parameters entering the simulation are listed in table 1. Using these time dependent rates, we simulate the time-dependent occupation probability for any microwave frequencies ω by evolving the rate equation

$$\begin{pmatrix} \frac{dn_1}{dt} \\ \vdots \\ \frac{dn_n}{dt} \end{pmatrix} = \begin{pmatrix} -\sum_{i=2}^n \Gamma_{i1}(t, \omega) & \Gamma_{12}(t, \omega) & \cdots & \Gamma_{n1}(t, \omega) \\ & \ddots & & \vdots \\ \Gamma_{21}(t, \omega) & & \ddots & \Gamma_{n-1n}(t, \omega) \\ \Gamma_{n1}(t, \omega) & \cdots & \Gamma_{nn-1}(t, \omega) & -\sum_{i=1}^{n-1} \Gamma_{in}(t, \omega) \end{pmatrix} \begin{pmatrix} n_1 \\ \vdots \\ n_n \end{pmatrix}, \quad [26]$$

starting from an arbitrary initial occupation distribution n_0 . To remove any dependence on the initial state, we let the system evolve until the norm of the difference between the occupation of one state during two consecutive periods is smaller than a tolerance value set between 10^{-5} and 10^{-7} . The time dependent current is then calculated from the evolution of the state occupations over the next 3 to 20 periods.

To speed up simulation time, we first simulate the rate equation for the lowest microwave frequency, where the system stays closest to its steady state solution (see S2.2): and choose therefore the steady-state distribution without drive as our initial state n_0 . For each consecutive frequency we then use the occupation of the closest, already simulated, frequency as the initial state.

S4 Methods

S4.1 Experimental setup

The measurements on the spin systems, i.e. individual Fe atoms and the 4-atom Fe chain, were performed using a low temperature, ultra-high vacuum scanning tunneling microscope (Unisoku USM-1300) with a ^3He cryostat, a (9/2/2) T superconducting vector magnet and high frequency wiring to the (PtIr)-tip. The measurements on the Yu-Shiba-Rusinov (YSR) state were performed using an ultra-low temperature, ultra-high vacuum scanning tunneling microscope (Unisoku USM-1600) with a dilution refrigerator and high frequency wiring to a bulk Vanadium-tip.

In all measurements, the low-frequency offset voltage was combined with the high-frequency microwave modulation using a bias-tee (Spin measurements: PSPL5575A-104, YSR measurements: Anritsu V251) and was applied to the tip-side of the tunnel junction. The frequency-dependent microwave modulation was produced by an arbitrary waveform generator (Keysight M8195m).

S4.2 Sample preparation

The sample surfaces were cleaned by repeated cycles of Ar^+ sputtering at 1 kV at a background pressure of $2 \cdot 10^{-6}$ mBar and subsequent annealing to several hundred K, respectively. The Cu(100) surface, for the measurements on the spin systems, was annealed at 850 K. The thin Cu_2N decoupling layer was grown by sputtering the surface at 1 kV in a N_2 atmosphere of $5 \cdot 10^{-6}$ mBar and consecutive annealing at 600 K. The V(100) surface, for the measurements on the YSR states, was annealed at 1073 K. For both substrates, Fe atoms were deposited onto the prepared and precooled sample surfaces (~ 20 K). The sample was positioned in front of a Knudsen cell evaporator with metallic Fe heated to 1300 K, for 8 s for the Cu_2N sample and 1500 K for 20 s for the V(100) sample.

S4.3 Atom manipulation

On the Cu_2N decoupling layer, Fe atoms occur naturally as individual atoms and can be identified by their spectroscopic features using conductance measurements [42]. Chains, consisting of multiple Fe atoms were assembled by picking up and placing Fe atoms via vertical manipulation. The Fe atoms in the chain are arranged 0.72 nm apart and parallel to the external magnetic field [21].